THESIS

CLOUD PROCESS INFORMATION FROM A FLEET OF SMALL SATELLITES: SYNTHETIC RETRIEVALS USING AN OPTIMAL ESTIMATION ALGORITHM

Submitted by

Richard M. Schulte

Department of Atmospheric Science

In partial fulfillment of the requirements

For the Degree of Master of Science

Colorado State University

Fort Collins, Colorado

Spring 2018

Master's Committee:

Advisor: Christian Kummerow

Michael Bell
Steven Reising

ABSTRACT

CLOUD PROCESS INFORMATION FROM A FLEET OF SMALL SATELLITES: SYNTHETIC RETRIEVALS USING AN OPTIMAL ESTIMATION ALGORITHM

The great importance of clouds in understanding atmospheric phenomena is widely recognized, yet faithful representations of cloud and precipitation processes in models at nearly all scales remain elusive. In order to properly constrain model parameters, it is important to obtain reliable observations of cloud properties in varying atmospheric environments. The Temporal Experiment for Storms and Tropical Systems (TEMPEST) mission was proposed to help address this need by deploying a cluster of CubeSats, each containing an identical, five-frequency passive microwave radiometer, into the same orbit. Doing so would allow for the observation of cloud processes at a high temporal resolution and on a global scale.

In order for such a mission to be useful in understanding cloud processes, it is crucial to develop a retrieval algorithm that can distinguish true changes in the atmospheric state from the noise induced by making repeated observations only a few minutes apart at different view angles. To this end, a physical optimal estimation algorithm is developed for the retrieval of water vapor, cloud water, and frozen hydrometeors from cross-track microwave sounders such as the TEMPEST radiometer. The performance of the algorithm is assessed by using high resolution Weather Research and Forecasting (WRF) model output to generate synthetic radiometer observations, while incorporating realistic error estimates, and then comparing the parameters retrieved using the synthetic observations to the actual model parameters.

For rapidly changing clouds, differences in parameters retrieved at various view angles, while not trivial, are small enough that changes in cloud properties can be discerned. This is especially true for view angles near nadir, where the field of view is smaller and changes less rapidly with time. Experiments simulating a cluster of TEMPEST instruments successively observing the same cloud system suggest that using the higher-quality retrievals near nadir to constrain preceding and subsequent observations allows for cloud changes to be observed more clearly. An analysis of the contribution of various forward model errors indicates that incorporating more accurate a-priori information about wind speed, cloud coverage, and cloud heights, perhaps obtained from coincident measurements by other spaceborne instruments, would further constrain the retrieval and mitigate some of the view angle induced biases.

ACKNOWLEDGEMENTS

I'd like to thank my advisor, Prof. Chris Kummerow, for his guidance throughout the course of this research. I'd also like to thank all of the members of the Kummerow group, but particularly Wes Berg and David Duncan, for many helpful discussions. Additionally, I am grateful for the helpful comments and insightful questions from my committee members, Professors Michael Bell and Steve Reising. Finally, I'd like to thank my siblings, Rory and Rebecca, and my parents, Kate and John, for their continual love and support. I feel very lucky to be part of an academic institution that not only produces first-class science, but that also allows me to live so close to my wonderful family.

TABLE OF CONTENTS

CHAPTER 1: INTRODUCTION

1.1 Motivation

Clouds are profoundly important in the atmospheric system. They link atmospheric and hydrologic processes, transfer moisture and momentum, affect large-scale circulations through latent heat release, and have radiative effects that strongly influence regional and global climate. Representing cloud processes remains one of the foremost challenges in atmospheric modeling. The spatial scales of cloud processes span several orders of magnitude, and most microphysical processes operate at scales much smaller than the grid box of a global climate model (GCM) or even the most detailed numerical weather forecast models. Thus parameterization is necessary to represent sub-grid scale processes in cloud resolving models (CRMs). Countless studies have shown that CRM output can be quite sensitive to the choice of cloud microphysics scheme or to the value chosen for certain parameters within a single scheme [e.g. *Saleeby and Cotton*, 2008; *Adams-Selin et al.*, 2013; *Cintineo et al*., 2014; *Van Weverberg et al*., 2014; *Morrison et al.*, 2015].

The value chosen for a given microphysical parameter can vary significantly from model to model and is often chosen by the modeler somewhat arbitrarily. Values chosen might be based on measurements from a single field campaign, even if the model is being applied to a different meteorological regime. In other cases, they might be chosen to maintain consistency with older studies, or parameter values might be chosen so as to “tune” a model to produce realistic-looking output fields. If representations of cloud and precipitation processes in models are to continue to improve, it is important to better constrain the appropriate choice of microphysical parameters and to gain a better understanding of how these parameters vary in different environments around the globe.

For example, one microphysical parameter that cloud models are particularly sensitive to, particularly for mixed-phase convective clouds, is the collection efficiency of liquid drops by ice and graupel. *Johnson et al.* [2015] used statistical emulation of the MAC3 cloud microphysics model to quantify the sensitivity of 12 cloud properties to aerosol concentrations and 9 microphysical model parameters. They found that, for a deep convective cloud, the model output was more sensitive to the graupel collection efficiency than to any other parameter, with the graupel collection efficiency having a particularly large effect on the amount of accumulated precipitation after 80 minutes and the maximum precipitation rate. Other cloud responses that were sensitive to collection efficiency included the mean cloud drop effective radius, the mean downdraft speed, the mean reflectivity, and the mean specific drop mass.

Clearly, an accurate estimate of this parameter is important if convective systems are to be simulated well in numerical weather prediction (NWP) models. Unfortunately, the parameter is not well-constrained or easily measured. The collection efficiency can depend on many factors, including the size and shape of the frozen particles and water drops, the relative collision velocity, and turbulence [*Khain et al*., 2000; *von Blohn et al*., 2009]. Moreover, it is not clear how other atmospheric parameters such as temperature or humidity may affect the collection efficiency.

Another parameter that is present in many microphysical schemes and that has been shown to be especially influential in the output of GCMs is the autoconversion threshold radius [e.g. *Lohmann and Feichter*, 1997]. When cloud droplets in a model are smaller than this radius, it is assumed that no cloud droplets collide to form larger drops and thus (in liquid-phase clouds) no precipitation is formed until the cloud droplets grow large enough through other processes such as condensational growth. This parameter is introduced to crudely mimic a widely observed characteristic of rain formation: that it tends to occur only once the coalescence process has been activated.

In GCMs, the autoconversion threshold radius has important impacts on cloud lifetimes and coverage. When the threshold radius is set to a higher value, rain formation is inhibited, leading to longer-lasting clouds and increased overall cloudiness. This can have important radiative consequences. As such, it is a parameter that is often tuned to ensure that climate models can properly simulate the radiation balance of the present day climate [e.g. *Rotstayn*, 2000]. In addition, the autoconversion threshold radius strongly influences the magnitude of aerosol indirect effects [*Golaz et al.*, 2011]. Figure 1.1, reprinted from *Golaz et al.* [2013], shows how changing the autoconversion threshold can significantly affect the amount of surface temperature warming in a GCM simulation. The GFDL CM3 coupled climate model was run with three different microphysical configurations, with the threshold radius ranging from 6.0 μm (red line) to 10.6 μm (blue line). Even though other cloud parameters were re-tuned for each run so as to achieve the same top-of-atmosphere radiation balance for the period 2001-2010, there are considerable differences in the model's simulation of 20th century surface temperatures for each configuration.

The model recreates the surface temperature record of the last 150 years with most fidelity when a threshold radius of 6.0 μm is used. However, this value is lower than what is supported by most observational studies. For example, *Pawlowska and Brenguier* [2003], analyzing flight segments from the Aerosol Characterization Experiment, found that it is only when the maximum mean volume droplet radius exceeds 10 μm that precipitation forms in stratocumulus clouds. *Suzuki et al*. [2013] similarly found that microphysical parameterizations in the GFDL CM3 that best reproduced satellite-observed microphysical statistics were not very skilled at reproducing simulated temperature trends, and that parameterizations which best reproduced temperature trends relied on parameter values inconsistent with observations. This disconnect between the constraints implied for the autoconversion threshold based on bottom-up process-based studies and top-down metrics such as the observed temperature trend suggests the presence of compensating errors in the model and underscores the fact that there is a lot of room for improvement in microphysical parameterizations.

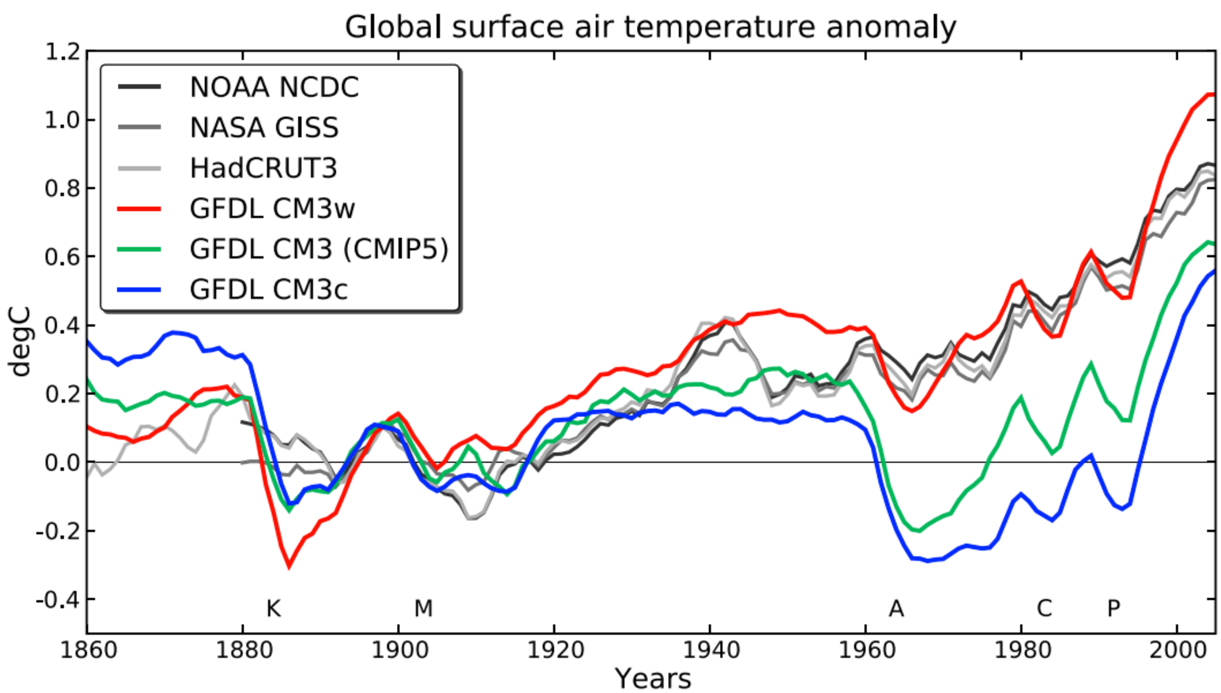

Figure 1.1. Time evolution of global mean surface air temperature anomalies from five-member ensemble runs of the GFDL CM3 climate model with different values chosen for the autoconversion threshold radius (6.0 μm in red, 8.2 μm in green, and 10.6 μm in blue) and additional cloud returning. Also plotted are observed temperature trends, and the letters above the horizontal axis mark major volcanic eruptions (cited from *Golaz et al.* [2013]).

1.2 Informing Cloud Models with High Temporal Resolution Satellite Observations

Comprehensive, multi-instrument field studies are one avenue for constraining model parameterizations, and can yield very accurate measurements for various parameters at a given place and time. However, they usually target one specific environment or type of cloud and often fail to give insight into how parameters might vary from one place to another. Satellite-based estimates of microphysical parameters, on the other hand, have larger uncertainties associated with them but can but used to construct global databases with which to examine relationships between microphysical parameters and large-scale environmental variables. Indeed, satellite instruments have been used for years to measure various cloud properties, with the goal of improving CRM parameterizations. For example, *Kawamoto et al.* [2001] developed a method by which to simultaneously measure cloud optical thickness and effective particle radius using Advanced Very High Resolution Radiometer (AVHRR) multispectral radiance data. *Suzuki et al.* [2010] made use of coincident measurements of vertical profiles of reflectivity from CloudSat and Moderate Resolution Imaging Spectroradiometer (MODIS) measurements of in-cloud optical depth and effective particle radius. They demonstrated a trimodal pattern in reflectivity profiles that they identified as corresponding to non-raining, drizzle, and raining precipitation categories and investigated their occurrence as a function of droplet size. *Suzuki et al.* [2011] then compared the observed satellite statistics with those produced by two CRMs, finding that models tend to convert cloud water to rain water too quickly and suggesting that deficient representations of autoconversion and accretion might be to blame.

Large, sophisticated satellite sensors such as CloudSat are clearly useful in measuring specific microphysical parameters with good accuracy. However, a downside is that a satellite in a typical orbit will observe any given cloud system at most once per orbit and often less frequently than that. It is thus hard to observe the temporal evolution of clouds to precipitation, and to measure the rate at which individual cloud processes occur. Propopsed geostationary microwave sounding instruments such as GeoSTAR [*Lambrigsten et al*., 2004] would in theory be able to observe changes in clouds on short timescales, but cost considerations have thus far precluded the launch of any microwave sounders into geostationary orbit. An alternative to a single, costly geostationary instrument is a constellation of much smaller satellites flying in low Earth orbit. The Temporal Experiment for Storms and Tropical Systems (TEMPEST) mission proposes to deploy a cluster of 6U-Class CubeSats, each carrying an identical five-frequency passive microwave radiometer, into the same orbital plane. The satellites would be spaced only a few minutes apart (this study assumes 6 CubeSats with 6-minute spacing) and thus would offer the opportunity to directly observe the lifecycle of clouds at a high temporal resolution, while also likely providing better spatial resolution than could be achieved by a radiometer in geostationary orbit.

The TEMPEST radiometers would not be able to provide the sort of detailed vertical profiles of clouds that more sophisticated sensors (such as the cloud radar on CloudSat) can provide. Nevertheless, by looking at the changes in measured radiances from one TEMPEST satellite to the next, as they observe the same scene, important information can be gathered about different processes taking place inside the clouds. For example, cloud water, rain water, ice, snow, and graupel each have radiometric signals in the part of the electromagnetic spectrum at which the TEMPEST radiometer operates. If TEMPEST radiometers are able to retrieve integrated amounts of cloud water and cloud ice, then changes in these values from one CubeSat overpass to the next could offer valuable insight into the rate at which cloud droplets are collected by frozen particles, and the rate at which clouds mature and transition to producing precipitation, in different large-scale environments. These observations, combined with modeling studies, could help constrain parameters such as the collection efficiency and autoconversion threshold. In addition, near-coincident measurements between the TEMPEST constellation and more sophisticated satellites such as CloudSat and the Global Precipitation Measurement (GPM) satellite would offer opportunities to leverage the temporal context provided by TEMPEST with more detailed microphysical information to further aid our understanding of cloud processes. CubeSats have the added benefit of being much cheaper to produce and to launch than traditional Earth observing satellites, with a much shorter development lifecycle.

As envisioned, the TEMPEST 6U CubeSats would be launched all at once into the same International Space Station (ISS) orbit, and then passive drag-adjusting maneuvers would be used to separate them by the desired amount. However, while the 6U CubeSats would all be in the same orbital plane, they would not sweep out identical footprints on the Earth, because the Earth would be rotating underneath them. This concept is illustrated qualitatively in Figure 1.2. Thus, it would be necessary to observe features at different view angles with each satellite pass. In order for this mission concept to be useful, then, it is critical to develop a retrieval algorithm that is as independent of view angle as possible. If two retrievals of, say, cloud liquid water path are performed over the same location a few minutes apart from each other and yield different results, one can only say something about the development of the cloud system if systematic biases due to view angle differences can be ruled out as the source of the discrepancy. In other words, the signal from the true change in atmospheric state must be larger than the noise introduced by taking two different measurements at different view angles. This thesis details the development of a robust optimal estimation retrieval algorithm for use with TEMPEST and other similar sensors and investigates the magnitude of sources of view-angle-induced errors.

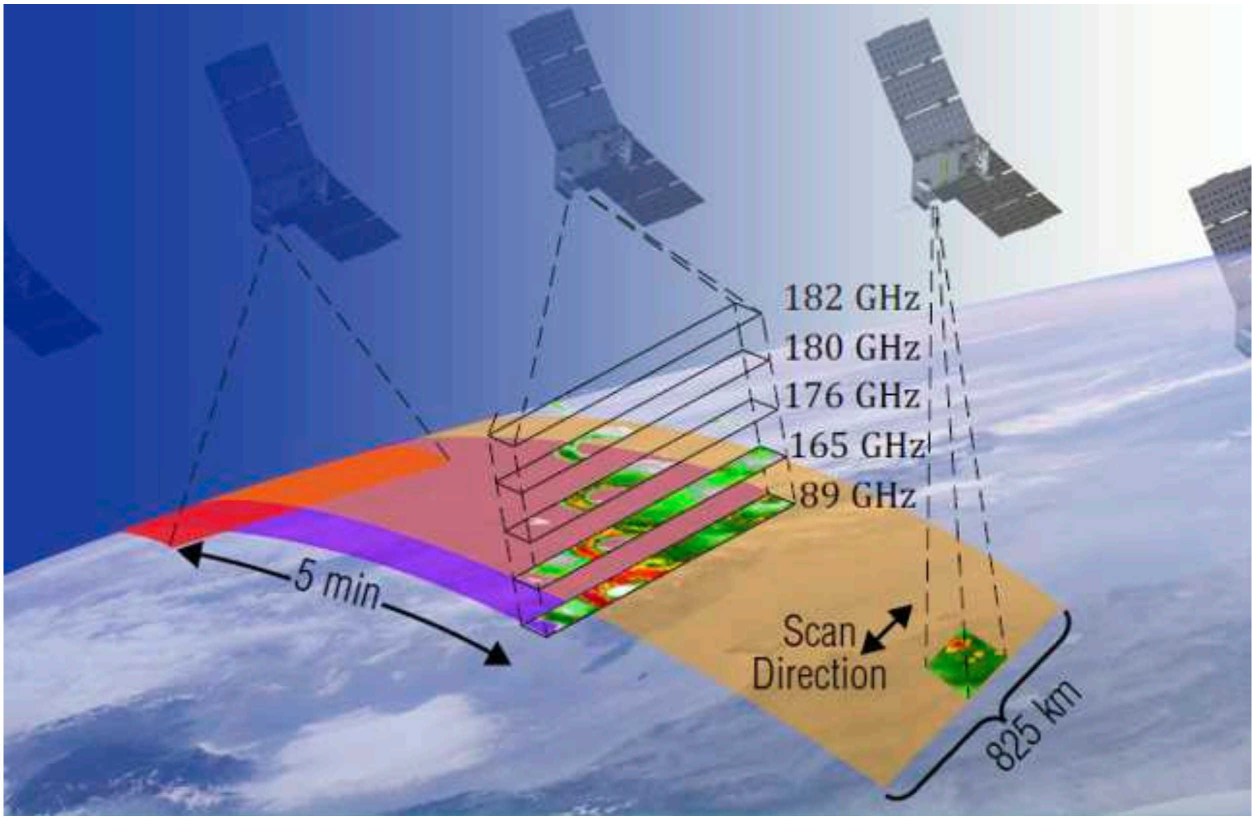

Figure 1.2. Conceptual illustration of the TEMPEST constellation of CubeSats (cited from *Reising et al.* [2017]).

CHAPTER 2: A ONE DIMENSION VARIATIONAL RETRIEVAL ALGORITHM FOR TEMPEST

2.1 Background

Spaceborne passive microwave radiometers have been used for over four decades to infer information about geophysical variables over the global oceans, beginning with the Nimbus 5 Microwave Spectrometer (NEMS) that operated at five frequencies between 22.235 and 58.8 GHz [*Staelin et al*., 1973]. Today, there are many satellites orbiting Earth that carry passive microwave radiometers as part of their payloads. These instruments operate with various frequency and polarization combinations. In all cases, they measure the amount of upwelling radiation at certain frequencies and from a certain direction that reach the satellite on which they are mounted.

Some of these passive microwave sensors, such as the Global Precipitation Measurement Microwave Imager (GMI), the Advanced Microwave Scanning Radiometer (AMSR), and the Special Sensor Microwave Imager / Sounder (SSMIS) series of instruments, are conically scanning. They view the Earth at a constant view angle with the same footprint size across the entire scan. These radiometers have channels at frequencies ranging from about 6 GHz to about 190 GHz. The fact that these instruments include channels at "window frequencies," where there is little absorption of radiation due to atmospheric constituents such as oxygen or water vapor, allows for the retrieval of surface characteristics such as sea surface temperature and wind speed. However, these instruments also have channels near the 22.235 GHz and 183.31 GHz water vapor absorption lines, which allow for the retrieval of total precipitable water (TPW) and some information about the vertical profile of water vapor in the atmosphere. Historically, instruments such as these have been termed “imagers” because of their skill in retrieving surface and column integrated variables, although this current generation of instruments does have limited sounding ability.

Other passive microwave radiometers, such as the Microwave Humidity Sounder (MHS), Advanced Microwave Sounding Unit (AMSU), Advanced Technology Microwave Sounder (ATMS), and the Sounder for Probing Vertical Profiles of Humidity (SAPHIR), are cross-track scanning. They view Earth at a range of view angles and footprint sizes. In most cases lacking the window channels of imagers, they are most adept at providing information about the vertical profiles of water vapor or temperature, rather than surface characteristics. For this reason they are termed “sounders.” Typically, a collection of frequencies between about 50 and 60 GHz is used for temperature sounding and frequencies on either side of the 183.3 GHz water vapor absorption line are used for moisture sounding.

The retrieval of atmospheric parameters from a collection of brightness temperature (T_b) measurements at different microwave frequencies is an example of an *inverse problem*. Given complete knowledge of the state of the atmosphere, it is relatively straightforward to use physical principles to model the amount of radiation at given frequencies that reaches a radiometer. In remote sensing terms, a *state vector* $\boldsymbol{x}$ containing information about the state of the atmosphere can be mapped to a *measurement vector* $\boldsymbol{y}$ representing the brightness temperatures at each frequency of interest through the use of a forward model, $\boldsymbol{f}$. However, in an atmospheric retrieval, it is the measurement vector that is known and we desire to solve for the state vector. Thus some method is required to allow one to solve for $\boldsymbol{x}$ as a function of $\boldsymbol{y}$ through the use of an inverse forward model, $\boldsymbol{f}^{-1}$. This is not an easy task, as radiative transfer cannot be well-represented with a linear forward model that would be easily inverted. The inverse problem is further complicated by the fact that it is *ill-posed*: two distinct atmospheric state vectors can yield very similar measurement vectors, making it harder to determine the true state of the atmosphere from a measurement vector alone (which will have measurement uncertainties associated with each of its components).

Many early passive microwave retrieval algorithms were regression-based [e.g. *Wilheit and Chang*, 1980; *Alishouse et al.*, 1990] or semi-physical methods that made assumptions to simplify the equations of radiative transfer in the atmosphere to make the inverse problem more tractable [*Greenwald et al.*, 1993; *Wentz*, 1997]. These early algorithms were sensor-specific, using derived equations to link T_bs at certain frequencies, or in some cases the difference in T_bs between two frequencies, to an estimate of the geophysical parameter of interest.

More recently, retrieval algorithms have been developed that make use of fully physical forward models, allow for the retrieval of all parameters of interest simultaneously, and are not tied to a specific sensor or set of frequencies. Algorithms of this type are better able to ensure that the retrieved atmospheric parameters are consistent with each other across sensors, and that, when put into a forward model, result in reasonable simulated brightness temperatures. Sensor-independent algorithms are desirable in that they allow for the creation of consistent records of geophysical variables across the ever-expanding history of spaceborne passive microwave radiometers. A common approach is to iteratively solve for a collection of geophysical parameters by repeatedly forward modeling the transfer of radiation through the atmosphere until a solution for the atmospheric state vector is found that yields forward modeled T_bs close to those observed by the satellite while also being consistent with prior knowledge (*a-priori* information) about the state of the atmosphere [*Deblonde and English*, 2003; *Elsaesser and Kummerow*, 2008; *Boukabara et al.,* 2011]. The Colorado State University 1-D variational (CSU

1DVAR) retrieval algorithm [*Duncan and Kummerow*, 2016] is one such algorithm, having initially been developed for the retrieval of non-raining parameters for GMI but having been adapted for use with other conically scanning instruments such as AMSR and the Tropical Rainfall Measuring Mission Microwave Imager (TMI). The work presented in this thesis demonstrates that the CSU 1DVAR algorithm can also be used to retrieve information from cross-track sounders.

2.2 Description of Spaceborne Sensors and Data

Specifically, this work applies the 1DVAR algorithm to the Temporal Experiment for Storms and Tropical Systems Technology Demonstration (TEMPEST-D) radiometer. TEMPEST-D is a 6U-class (34 cm by 20 cm by 10 cm) CubeSat that is planned to be launched into the ISS orbit in 2018. The ISS orbit has an altitude of about 400 km with an inclination of 51.64 degrees and a period of 92.65 minutes. TEMPEST-D is meant to demonstrate the drag-adjusting maneuvers that will be necessary to provide time separation for a train of CubeSats and to demonstrate precision intercalibration between TEMPEST-D measurements and those made by other spaceborne passive microwave radiometers. Thus it will reduce the risk, cost, and development time for future CubeSat constellation missions, including TEMPEST. It will carry a five-frequency, cross-track scanning passive radiometer, with channel frequencies centered near 89, 165, 176, 180, and 182 GHz. Although this work focuses on synthetic TEMPEST retrievals in preparation for the launch of TEMPEST-D, the algorithm can be easily adapted for use with other cross-track sounders, such as MHS, which operate at similar frequencies. Table 2.1 gives detailed specifications for TEMPEST-D and MHS.

Table 2.1 Selected sensor specifications for TEMPEST-D and MHS. QV polarization is quasi-vertical (i.e., vertical polarization at nadir) and QH is quasi-horizontal. NEDT and IFOV are abbreviations for Noise Equivalent Differential Temperature and Instantaneous Field of View, respectively.

	Channel Frequency (GHz)	Polarization	NEDT (K)	Beamwidth (degrees)	Nadir IFOV (km)	Edge IFOV – Across Track (km)	Edge IFOV – Along Track (km)
TEMPEST-D:							
	89	QV	0.3	3.6	25.1	55.8	36.8
	165	QV	0.5	1.8	12.6	27.9	18.4
	176	QV	0.6	1.8	12.6	27.9	18.4
	180	QV	0.7	1.8	12.6	27.9	18.4
	182	QV	0.9	1.8	12.6	27.9	18.4
MHS:							
	89	QV	0.22	1.12	15.9	52.8	27.1
	157	QV	0.34	1.17	15.9	52.8	27.1
	183.3 ±1.0	QH	0.51	1.05	15.9	52.8	27.1
	183.3 ±3.0	QH	0.40	1.02	15.9	52.8	27.1
	190.3	QV	0.46	1.02	15.9	52.8	27.1

Output from the Weather Research and Forecasting (WRF) mesoscale numerical weather prediction model [*Michalakes et al.*, 2001] using the Advanced Research WRF (ARW) dynamical core and the WDM6 microphysics scheme [*Lim and Hong*, 2010] is used to generate synthetic TEMPEST observations. The model output comes from a simulation of Hurricane Gonzalo, which formed in the Atlantic Ocean in October 2014. The simulation covers the time period from 0600 to 1800 UTC on October 16, 2014, with model output available every 3 minutes. The horizontal resolution is 3 km and the model has 30 vertical levels, using sigma coordinates. The domain stretches roughly from 74°W to 63°W and from 21°N to 29°N. The model output is converted to T_bs at the TEMPEST-D frequencies using the radiative transfer model described in Section 2.3.

This particular simulation was chosen for this study mostly because of its high spatial and temporal resolution. This allows us to determine whether T_b differences due to changing atmospheric conditions on short time scales are sufficiently larger than T_b differences due to view angle differences, so as to confidently diagnose cloud changes occurring between

TEMPEST satellite measurements. Another benefit of the simulation is that it includes a variety of atmospheric conditions, from clear-sky conditions outside the radius of the storm to spotty clouds on the periphery of the storm to heavy rain in the center of the storm. The outer bands of the storm offer a good opportunity to test the retrieval algorithm's performance in the case of clouds rapidly developing and transitioning to precipitation. However, the fact that a tropical cyclone simulation is used should not lead the reader to believe that TEMPEST-D or the full TEMPEST mission is specifically designed to observe tropical cyclones. In fact, near the center of a tropical cyclone, where precipitation is very heavy, it is unlikely that a passive radiometer like TEMPEST would be able to determine cloud properties with much accuracy.

Ancillary data (sea surface temperatures, surface wind speeds, surface pressures, and temperature profiles) used by the retrieval algorithm are taken from the European Center for Medium-Range Weather Forecasts' reanalysis product, ERA5. The reanalysis data have a temporal resolution of 1 hour and a horizontal spatial resolution of 30 km, with 137 vertical levels. A-priori information about the atmospheric state is also taken from ERA5. Using ERA5 for a-priori and ancillary data has limitations. The data have to be interpolated to match the much finer temporal and spatial resolution of the WRF model. Also, the ERA5 product is not designed to be particularly skillful at reproducing tropical cyclones, so in some cases the errors between the ERA5 state and the WRF model output can be quite large. For example, ERA5 underestimates the wind speed near the center of the hurricane compared to WRF, and many of the finer structures in the rain bands are missed. In operational use, it might be possible to make use of more sophisticated methods of obtaining a-priori and ancillary information to slightly improve the retrieval algorithm. However, even though errors can be quite large at certain pixels, this is explicitly accounted for in the calculation of the a-priori and forward model error covariance matrices (see Section 2.4.3).

2.3 Generation of Synthetic TEMPEST Observations

In order to create the synthetic TEMPEST "observed" T_bs used to test the retrieval algorithm, the full 30-level WRF model profiles from the simulation of Hurricane Gonzalo, without any simplifying assumptions or interpolation, are run through a radiative transfer model. The ray tracing makes uses of actual three-dimensional geometry to create synthetic T_bs for view angles ranging from nadir to 45 degrees, and then a small number randomly sampled from a Gaussian distribution with a mean of zero and a standard deviation of 1K is added to each T_b value to simulate the sensor noise that will be present in the actual TEMPEST-D instrument.

The *Rosenkranz* [1998] model is used for atmospheric gaseous absorption by oxygen, nitrogen, and water vapor. The surface emissivity and reflectivity are calculated from the FASTEM6 ocean surface emissivity model [*Kazumori and English*, 2015]. Absorption and scattering due to cloud liquid water are calculated using Mie theory, with cloud droplets and rain drops assumed to be spherical with sizes following the same gamma distributions assumed by the WDM6 microphysics scheme (equation 1 in *Lim and Hong* [2010], with a shape parameter of 3 for cloud droplets and a shape parameter of 1 for rain). Graupel particles are assumed to follow an exponential size distribution (equation 1 in *Hong and Lim* [2006]), and scattering properties are similarly calculated using Mie theory. The density of all graupel particles is assumed to be 500 g/cm^3, as in WDM6.

The WDM6 microphysical scheme has two additional classes of frozen hydrometeors, deemed "ice" and "snow." Ice particles are typically smaller than snow particles (most are less than 500 microns in maximum dimension) and more dense. However, the distinction between the two categories can be fuzzy, and both species are therefore included as part of the ice water path that the 1DVAR algorithm tries to retrieve, while graupel is kept as a distinct ice water species. Thus, it is worth examining more closely how the size distributions for ice and snow are specified in WDM6.

The number concentration of ice particles, N_I, is treated differently in WDM6 than it is in most other bulk microphysical schemes. For any given level of the atmosphere at any given grid point, N_I is diagnosed based on the mixing ratio of ice present:

$$N_I = 5.38 \times 10^7 (\rho q_I)^{0.75} \tag{2.1}$$

where ρ is the density of the air and q_I is the mixing ratio of ice. This equation comes from equating two different parameterizations for the fall speed of cloud ice, the first from *Heymsfield and Donner* [1990] relating the mean fall speed to the ice mixing ratio and the second from *Heymsfield and Iaquinta* [2000] relating the fall speed of a single ice particle to its diameter. In this framework, all of the ice particles within a given grid box are assumed to have the same size with a maximum dimension given by

$$D_I = \left(\frac{\rho q_I}{2.08 \times 10^{22}}\right)^{0.125} \tag{2.2}$$

Notably, while mechanisms exist within the WDM6 scheme to move mass from the ice category to the snow category, there is no size threshold at which ice is automatically converted into snow (unlike many other bulk microphysical schemes), which can sometimes result in "ice" particles that are comparable in size to or even larger than some of the "snow" particles.

Snow particles, on the other hand, follow an exponential distribution:

$$N_S(D) = N_0 \exp{(-\lambda D)} \tag{2.3}$$

Here $N_S(D)$ is the number concentration (in m^{-4}) of snow particles of maximum dimension D, N_0 is the intercept parameter, and the slope λ is determined based on the snow mixing ratio and N_0:

$$\lambda = (\frac{N_0 \rho_S \pi}{\rho q_s})^{0.25} \tag{2.4}$$

where ρ_s is the density of snow (a constant 100 g/cm^3 in WDM6) and q_s is the mixing ratio of snow. The intercept parameter N_0 is not constant but has a dependence on temperature, meant to represent the broadening of snow distributions that is observed at higher temperatures. Thus,

$$N_0 = \min\{2\times10^8, 2\times10^6 \times \exp[0.12(T_0 - T)]\} \tag{2.5}$$

The WDM6 scheme does not specify the crystal habit, or shape, of the ice and snow particles. In past decades, it has been common to model ice particles as low-density (sometimes called "fluffy" or "soft") spheres [e.g., *Zhao and Wang,* 2002] and use Mie theory. However, it is now widely recognized that doing so introduces significant errors [e.g., *Kulie et al.*, 2010]. In more recent years, several groups have used modeling studies to produce single-scattering properties in the microwave regime for various non-spherical habits [e.g., *Hong,* 2007; *Kim et al.,* 2007; *Petty and Huang,* 2010]. For the purpose of generating synthetic TEMPEST observations, any habit(s) could be defined to be the "truth," including soft spheres; however, it is probably more helpful in terms of testing the retrieval algorithm to make more realistic assumptions. This work makes use of a database of microwave scattering properties for ice particles [*Liu*, 2008] as well as an associated database for larger aggregates of ice crystals [*Nowell et al.*, 2013]. These databases use the discrete dipole approximation method (DDA; see *Draine and Flatau* [2000]) to compute single-scattering properties by approximating a continuum target with a finite array of polarizable points. Habits are chosen that have mass-diameter relationships that mostly closely resemble the relationships in WDM6: thus, ice particles are treated as "long columns" (*Liu* shape 0) and snow particles as aggregates of 200 μm and 400 μm rosettes (*Liu* shape 13) for the purposes of calculating scattering properties in the radiative transfer model.

Using this radiative transfer model, brightness temperatures are calculated at the 3 km by 3 km resolution specified by the WRF model. Then, these T_bs are averaged across the field of view (FOV) of the satellite, using a two-dimensional Gaussian weighting function. The FOV is calculated based on the beamwidth of the radiometer, as well as the view angle and the height of the satellite orbit. Since precise orbital parameters for TEMPEST are not known, simplified geometry is used that assumes a locally flat earth and a constant orbit height of 400 km. In this formulation, the cross-track and along-track fields of view are given by FOV_{CT} and FOV_{DT}, respectively:

$$\mathrm{FOV}_{CT} = \mathrm{H}(\tan\left(\alpha + \frac{\beta}{2}\right) - \tan\left(\alpha - \frac{\beta}{2}\right)) \tag{2.6}$$

$$\mathrm{FOV}_{DT} = \frac{2\mathrm{H}}{\cos(\alpha)} \tan\left(\frac{\beta}{2}\right) \tag{2.7}$$

where H = 400 km is the height of the satellite, α is the view angle, and β is the beamwidth in degrees. For the 89 GHz channel on TEMPEST, β is 3.6, while for the other channels it is 1.8. This simplified method of calculating the FOV does lead to small errors on the order of a few km at the edge of the scan, but should be adequate for estimating the FOV-induced errors in the retrieval algorithm.

2.4 CSU 1DVAR

The 1DVAR technique, also known as optimal estimation, is a regularized matrix inverse method based on Bayes' Theorem. Much of the mathematics that follows is laid out more explicitly in other texts, such as *Rodgers* [2000]. As mentioned above, the relationship between the physical state of the atmosphere and measured T_bs can be generalized by the following expression:

$$\boldsymbol{y} = \boldsymbol{f}(\boldsymbol{x}, \boldsymbol{b}) + \boldsymbol{\varepsilon} \tag{2.8}$$

where $\boldsymbol{y}$ is the measurement vector containing the observed T_bs at each radiometer channel and $\boldsymbol{x}$ is the state vector containing the atmospheric properties to be estimated. In the case of TEMPEST, the state vector contains five parameters: the three leading principal components (PCs) of the water vapor profile, the integrated amount of liquid cloud water in the atmospheric column (LWP), and the integrated amount of cloud ice and snow (IWP). However, to calculate simulated T_bs, the forward model $\boldsymbol{f}$ depends not only on the parameters in the state vector but also on a variety of parameters not solved for but assumed to be known in the model atmosphere (for example, surface temperature, surface wind speed, vertical profile of temperature, cloud height and depth, etc.) These parameters are included in the vector $\boldsymbol{b}$. Finally, $\boldsymbol{\varepsilon}$ is an error term containing uncertainties due to sensor noise, errors in the forward model, and uncertainties in the forward model parameter assumptions ($\boldsymbol{b}$). The forward modeled T_bs $\boldsymbol{f}(\boldsymbol{x}, \boldsymbol{b})$ should agree with the satellite measurements $\boldsymbol{y}$ within the model and sensor error estimates given by $\boldsymbol{\varepsilon}$. The aim of the 1DVAR algorithm is to find the most likely state vector $\boldsymbol{x}$, given measurements $\boldsymbol{y}$, prior knowledge about the state of the atmosphere, and proper error estimates.

The most likely state vector is found by making use of probability density functions (PDFs) and Bayes' theorem. According to Bayes' theorem, the conditional probability $P(\boldsymbol{x}|\boldsymbol{y})$ of state $\boldsymbol{x}$, given measurements $\boldsymbol{y}$, is equal to

$$P(\boldsymbol{x}|\boldsymbol{y}) = \frac{P(\boldsymbol{y}|\boldsymbol{x})P(\boldsymbol{x})}{P(\boldsymbol{y})} \tag{2.9}$$

where $P(\boldsymbol{y}|\boldsymbol{x})$ is the probability of $\boldsymbol{y}$ given $\boldsymbol{x}$, $P(\boldsymbol{x})$ is the PDF of the state vector, and $P(\boldsymbol{y})$ is the PDF of the measurement vector. Our goal is to maximize $P(\boldsymbol{x}|\boldsymbol{y})$ for a particular $\boldsymbol{y}$. Equivalently, since $P(\boldsymbol{y})$ is independent of $\boldsymbol{x}$, the aim is to maximize the product $P(\boldsymbol{y}|\boldsymbol{x})P(\boldsymbol{x})$.

Now, let us assume that the values of the parameters in $\boldsymbol{x}$ are distributed in a Gaussian fashion. This is a reasonable assumption for the water vapor profile coefficients. LWP and IWP do not tend to be Gaussian-distributed in nature, so instead the parameters $\log_{10}$(LWP) and $\log_{10}$(IWP) are used. This makes their distributions more Gaussian, although it is still not a perfect assumption (since, in cloud-free conditions, the LWP and IWP will always be equal to zero). Under this assumption, $P(\boldsymbol{x})$ can be expressed by

$$P(\boldsymbol{x}) = \frac{1}{(2\pi)^{m/2}|\boldsymbol{S_a}|} \exp\left[-\frac{1}{2}(\boldsymbol{x}-\boldsymbol{x_a})^T \boldsymbol{S_a}^{-1}(\boldsymbol{x}-\boldsymbol{x_a})\right] \tag{2.10}$$

where m is the number of elements in $\boldsymbol{x}$, $\boldsymbol{x_a}$ is an estimate of the state vector independent of the satellite measurements (the *a-priori state vector*), and $\boldsymbol{S_a}$ is the associated error covariance matrix, obtained empirically. Similarly, we assume that the statistics of the measurements are also Gaussian, so that we can state

$$P(\boldsymbol{y}|\boldsymbol{x}) = \frac{1}{(2\pi)^{mn/2}|\boldsymbol{S_y}|} \exp\left[-\frac{1}{2}(\boldsymbol{y}-\boldsymbol{f}(\boldsymbol{x},\boldsymbol{b}))^T \boldsymbol{S_y}^{-1}(\boldsymbol{y}-\boldsymbol{f}(\boldsymbol{x},\boldsymbol{b}))\right] \tag{2.11}$$

Here n is the number of elements in $\boldsymbol{y}$, and $\boldsymbol{S_y}$ is the measurements/forward model error covariance matrix. $\boldsymbol{S_y}$ is, essentially, a matrix representation of the error term $\boldsymbol{\varepsilon}$, with the errors assumed for each radiometer channel as the main diagonal elements of the matrix and covariances of the errors between the channels as the off-diagonal elements.

Combining equations 2.10 and 2.11, it can be seen that maximizing the product $P(\boldsymbol{y}|\boldsymbol{x})P(\boldsymbol{x})$ amounts to maximizing

$$\exp\left[-\frac{1}{2}(\boldsymbol{x}-\boldsymbol{x_a})^T \boldsymbol{S_a}^{-1}(\boldsymbol{x}-\boldsymbol{x_a})\right] \cdot \exp\left[-\frac{1}{2}(\boldsymbol{y}-\boldsymbol{f}(\boldsymbol{x},\boldsymbol{b}))^T \boldsymbol{S_y}^{-1}(\boldsymbol{y}-\boldsymbol{f}(\boldsymbol{x},\boldsymbol{b}))\right].$$

This will occur when the cost function, Φ, is minimized, with Φ defined as follows:

$$\Phi = (\boldsymbol{x} - \boldsymbol{x_a})^T \boldsymbol{S_a}^{-1} (\boldsymbol{x} - \boldsymbol{x_a}) + [\boldsymbol{y} - \boldsymbol{f}(\boldsymbol{x}, \boldsymbol{b})]^T \boldsymbol{S_y}^{-1} [\boldsymbol{y} - \boldsymbol{f}(\boldsymbol{x}, \boldsymbol{b})] \tag{2.12}$$

The cost function thus weights both measurements and prior knowledge, in relation to their uncertainties. The first term in the cost function penalizes a potential solution vector $\boldsymbol{x}$ for departures from the fixed a-priori state vector values. This prevents the algorithm from settling on a state vector that might match observed T_bs quite well but that is physically unrealistic. The second term in the cost function penalizes potential solution state vectors whose forward computed T_bs differ substantially from the satellite-observed T_bs. This term, normalized by the number of satellite channels used, can also be called the chi-squared metric:

$$\chi^2 = [\boldsymbol{y} - \boldsymbol{f}(\boldsymbol{x}, \boldsymbol{b})]^T \boldsymbol{S_y}^{-1} [\boldsymbol{y} - \boldsymbol{f}(\boldsymbol{x}, \boldsymbol{b})]/n \tag{2.13}$$

The χ^2 value measures the quality-of-fit between the forward modeled T_bs and the observations, independent of departures from the a-priori state vector. That is, the lower the χ^2 value, the greater the consistency between the state vector and the satellite observations.

Minimizing Φ and finding the maximum probability state vector $\boldsymbol{x}$ is accomplished by finding the value for $\boldsymbol{x}$ at which the gradient of the cost function, $\nabla_x \Phi$, is equal to zero. Because the forward model is non-linear, this value cannot be solved for explicitly. Instead, the Gauss-Newton method of iteration is used. Starting with some first guess for the state vector, $\boldsymbol{x_i}$, new guesses are found via the following equation:

$$\boldsymbol{x}_{i+1} = \boldsymbol{x}_i + (\boldsymbol{S_a}^{-1} + \boldsymbol{K}_i^T \boldsymbol{S_y}^{-1} \boldsymbol{K_i})^{-1} \left[\boldsymbol{K_i}^T \boldsymbol{S_y}^{-1} \left(\boldsymbol{y} - \boldsymbol{f}(\boldsymbol{x}, \boldsymbol{b})\right) - \boldsymbol{S_a}^{-1} (\boldsymbol{x_i} - \boldsymbol{x_a})\right] \tag{2.14}$$

where $\boldsymbol{x}_{i+1}$ is the state vector after $i + 1$ iterations. $\boldsymbol{K}$ is a matrix of derivatives (Jacobian) containing the change in the forward modeled T_bs at each measurement frequency resulting from perturbations to the state vector (that is, $K_{ij} = \frac{\partial f_i}{\partial x_j}$). As $\boldsymbol{f}$ is non-linear, $\boldsymbol{K}$ is re-computed each iteration so as to linearize the problem about the current value of $\boldsymbol{x}$. Convergence is achieved once there is very little change between iterations (equation 5.29 in *Rodgers* [2000]).

2.4.1 Forward Model

The forward model used in the TEMPEST 1DVAR retrieval makes use of the same basic radiative transfer code that is used to create the synthetic brightness temperatures as described in Section 2.3; however, several simplifying assumptions are made. These assumptions serve to speed up the code but, perhaps more importantly for this exercise, introduce errors into the forward model that mimic the type of errors that one would expect to be present if real data were being used. After all, a forward model set up in exactly the same manner would be able to reproduce the synthetic brightness temperatures exactly (at least, to within the amount of random noise artificially imposed at the end of the process), but in reality no forward model will ever be able to exactly model the true atmosphere. The setup of this experiment retains nearly all of the major sources of forward model error that we expect to be present for the true TEMPEST-D mission. The only notable exceptions are errors due to the surface emissivity and water vapor absorption models, since the exact same models are used both to generate the synthetic TEMPEST observations and to calculate brightness temperatures in the 1DVAR forward model. However, emissivity model errors are not expected to be much of a problem due to the fact that only one of the TEMPEST channels (89 GHz) has meaningful sensitivity to the surface. Most contemporary models of water vapor absorption are thought to be largely accurate, so clear-sky absorption errors should similarly be dwarfed by the other sources of error considered in this study.

Instead of the 30 vertical levels in the WRF output, the forward model makes use of 16 vertical pressure layers, with 50 hPa layer depths from 300 hPa to the surface and additional layers from 100-200 hPa and 200-300 hPa. This configuration is slightly different than that used in *Duncan and Kummerow* [2016], which had better vertical resolution from 900 hPa to the surface but worse from 300-500 hPa. The change in layer spacing allows the retrieval to make better use of the information provided by TEMPEST about the middle atmosphere, where most of the weighting functions for the TEMPEST frequencies peak.

The input values required by the forward model include the following: the sea surface temperature (SST); surface wind speed; surface pressure; height and temperature of each layer in the atmospheric column; LWP and IWP; and the average water vapor pressure in each layer. The SST, wind speed, surface pressure, and height and temperature profiles are taken from the interpolated ERA5 reanalysis product. These values do not change from one iteration of the retrieval to the next. The a-priori values for LWP, IWP (combining both ice and snow particles), and the water vapor profile are also taken from ERA5, but these values do change as the algorithm works to find the optimal solution that minimizes the cost function.

The forward model makes the plane-parallel assumption, meaning that the atmosphere is assumed to have no horizontal variation at any given pressure level. Another important assumption is that of fixed cloud levels. In the forward model, all of the cloud water is assumed to be distributed evenly between 800 and 900 hPa, following *Duncan and Kummerow* [2016]. This approach obviously has limitations since clouds in the real atmosphere can and do form outside these levels. However, errors in the simulated T_bs caused by this simplistic representation are somewhat mitigated by the fact that the emissivity of liquid cloud drops increases with decreasing temperature [*Matzler et al.*, 2010]. The implication is that the effective emission is tied much more closely to the total amount of liquid water in the column than it is to cloud height. Various other methods of distributing the cloud water in a fixed manner in the forward model were tested; however, without reliable a-priori information about the heights and depths of the clouds, the effect on the overall accuracy of the cloud water retrieval is small. The effects of this fixed cloud layer assumption are examined more thoroughly in Chapter 4.

More care should be taken with the vertical placement of cloud ice. Most of the effect on T_bs due to ice comes from scattering. Ice particles present at different levels of the atmosphere (and thus at different temperatures) tend to have different particle size distributions (PSDs), leading to different scattering effects. In this study, cloud ice is distributed among the upper levels of the forward model atmosphere according to a constant ratio determined by calculating the average amount of cloud ice at each level for all pixels in the Hurricane Gonzalo WRF simulation that have a total IWP above 10 g/m^2. The exception is that cloud ice is not allowed to occur at temperatures above 273 K. This method seeks to minimize the overall bias in the retrieval of IWP, although errors due to the vertical placement of cloud ice can still be quite large for individual pixels.

The forward model assumes a monodisperse drop size distribution (DSD) for liquid cloud water with spherical particles of radius 15 μm. In reality, cloud particles are not monodisperse nor are they precisely spherical, but this should not be a large cause for concern because most non-precipitating cloud droplets are small enough that scattering is negligible and absorption is largely dependent on the total mass of water in the cloud, not the DSD [*Bennartz*, 2007].

Once again, things are much more difficult when it comes to ice, as assumptions made in regard to both ice crystal habit and size distribution can have a large effect on forward modeled brightness temperatures. To demonstrate the dramatic effect that ice crystal habit can have on microwave brightness temperatures, a series of experiments were conducted in which a sample atmospheric profile was run through the forward model, first with no ice and then with an IWP of 1 kg/m^2, to produce brightness temperatures at the TEMPEST frequencies. The surface characteristics and vertical profiles of water vapor, temperature, and geopotential height were set to the average values for all pixels in the Hurricane Gonzalo simulation, the LWP was set to 0 g/m^2, and the assumed view angle was a moderate value of 20 degrees. In each experiment a different ice habit was assumed. The experiments all assumed a monodisperse PSD (with ice particle diameters of either 400 μm or 1 mm), to isolate the effect of different particle habits from the effect of different PSDs.

Figure 2.1 shows the difference between the clear-sky T_b and the cloudy-sky T_b at two frequencies, 89 GHz and 165 GHz. Results for the 176, 180, 182 GHz channels are not shown because they are quite similar to the results at 165 GHz. For small ice particles at 89 GHz, where the wavelength of radiation (about 3.4 mm) is an order of magnitude larger than the diameter of 400 micron particles, scattering is limited and the difference among the various habits is negligible. For larger particles, however, and especially at the higher frequency (i.e. shorter wavelength) TEMPEST channels, it is clear that there are large differences in the T_b response among the different habits. For 400 μm particles at 165 GHz, the difference in brightness temperature between the clear-sky and cloudy-sky case ranges from 7.0 K for 4-bullet rosettes to 52.8 K for block columns with a standard deviation of 15.0 K among the different habits. For particles with diameter 1 mm, the differences are even more stark. The spread in T_b depression at 89 GHz for 400 micron particles ranges from 16.2 K on the low end (for a soft sphere of density 100 g/cm^3) to a whopping 174.7 K at the high end. Even ignoring the block column and solid sphere categories, which probably aren't very realistic for a particle of this size, the range

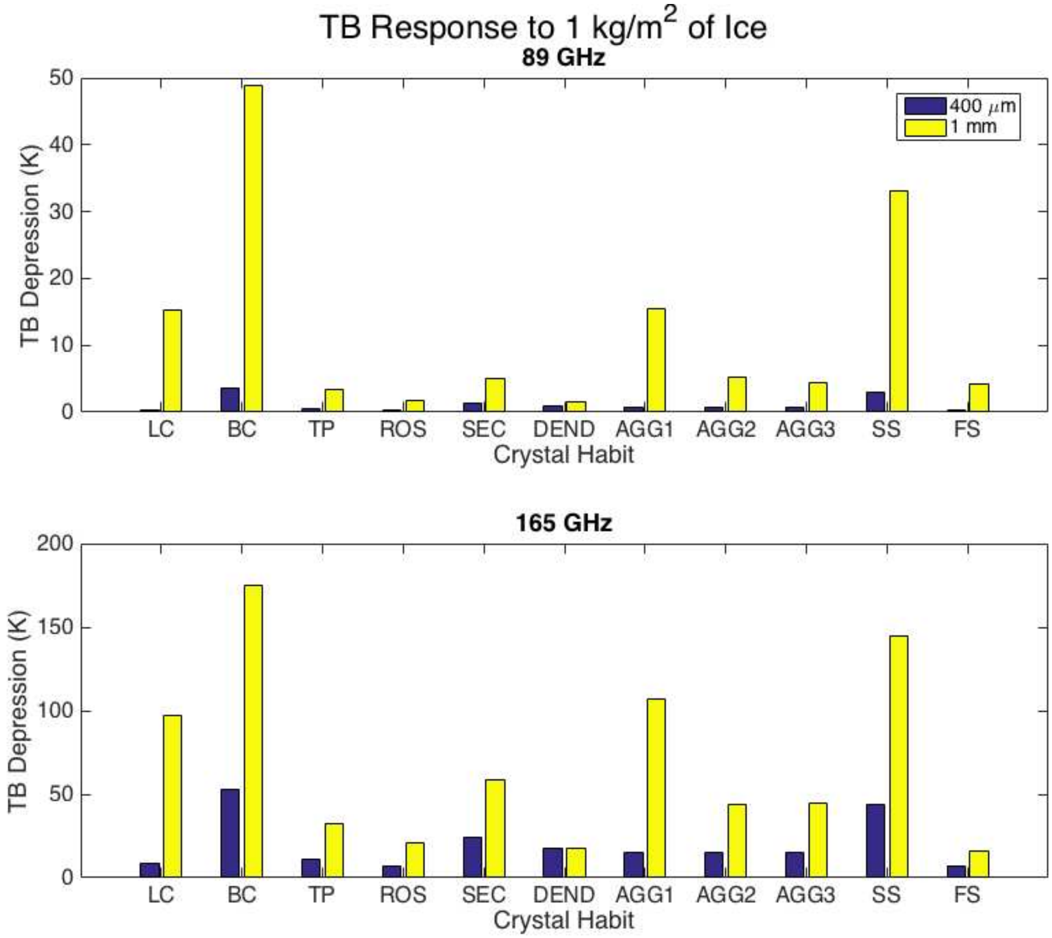

Figure 2.1. Clear-sky T_b minus cloudy-sky T_b at 89 GHz (top) and 165 GHz (bottom) for a variety of ice habits with a fixed IWP of 1 kg/m^2. Results are shown for monodisperse distributions of ice particles with diameters of 400 μm (blue) as well as 1 mm (yellow). The crystal habits included (as named in *Liu* 2008 and *Nowell et al*., 2013) are as follows: long column (LC); block column (BC); thin plate (TP); 4-bullet rosette (ROS); sector snowflake (SEC); dendrite snowflake (DEN); aggregate of 200 μm, 6-bullet rosettes (AGG1); aggregate of 400 μm, 6-bullet rosettes (AGG2); and aggregate of 200 and 400 μm, 6-bullet rosettes (AGG3). Also shown are results from explicit Mie theory calculations using solid spheres (SS) or low-density fluffy spheres (FS).

between assuming soft spheres and assuming aggregates of 200 μm rosettes spans more than 100 K, with a standard deviation of 33.6 K. In general, habits that assume a higher density for the ice particles tend to produce more extinction, though this is not uniformly true. For example, block columns cause a greater T_b depression than solid spheres, even though they have less than half the density. Note also that, while for most habits increasing particle size leads to increasing extinction, the effect is not uniform across all particle habits; in fact, for dendrites there is actually less extinction when the particles are assumed to be 1 mm in diameter than when they are assumed to be 400 μm.

The ice PSD can also have a large effect on the TB response. To illustrate this, another set of experiments was performed with the sample atmospheric profile in which the ice crystal habit was kept constant (Liu aggregates were used), but different PSDs were specified. Figure 2.2 shows the TB response at 89 GHz and 165 GHz for IWP ranging from 0 to 2000 g/cm^3. Clearly, there is less scattering when the WDM6 ice distribution (green) is used as compared to the other size distributions, but even among the other distributions, the differences in TB response can be on the order of 20 K for large amounts of cloud ice. When the temperature of the cloud is adjusted, these differences can be magnified even further (not shown).

When selecting a PSD and crystal habits to use in the forward model, a priority was placed on selecting a scheme that was both flexible (i.e. applicable to a variety of regimes) and grounded in observations. Maintaining consistency with the scheme used to generate the synthetic TEMPEST observations would be counter-productive, in that the WDM6 microphysics scheme is designed for speed of computation and is known to have deficiencies, particularly with respect to ice [e.g., *Van Weverberg et al.*, 2013]. Moreover, as mentioned above, no PSD is going to be a perfect representation of the real atmosphere, and so if realistic estimates of the

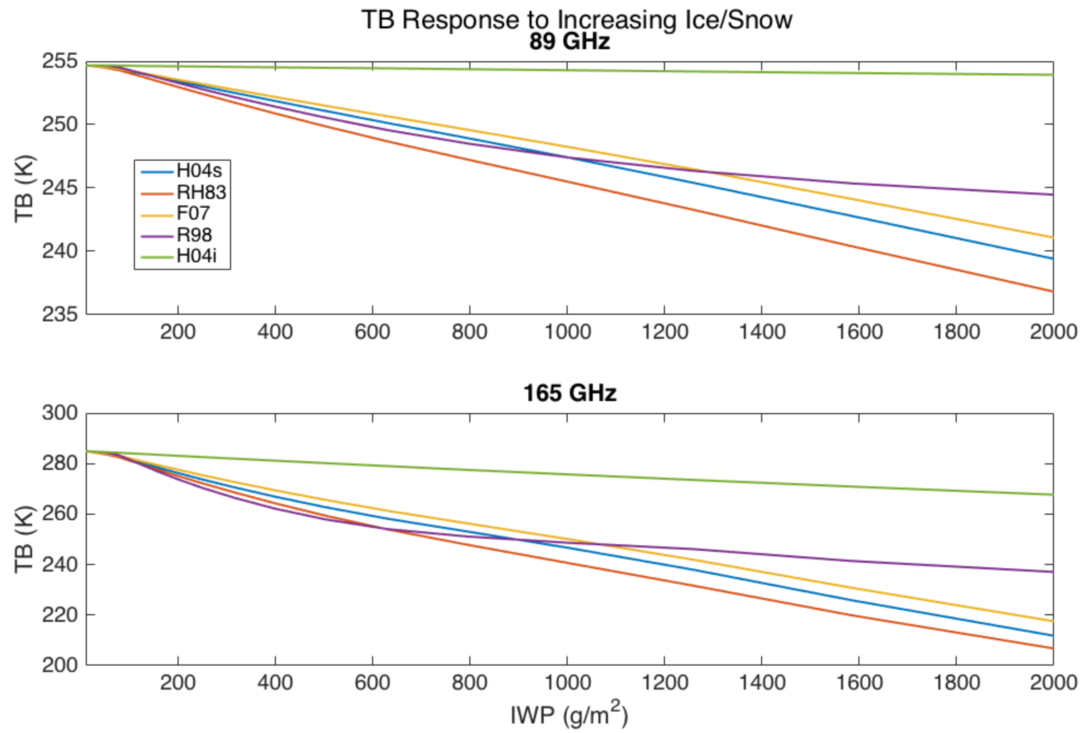

Figure 2.2. 89 GHz (top) and 165 GHz (bottom) T_bs as a function of IWP for different assumed ice PSDs. The PSDs tested include: (*blue, H04s*) WDM6 snow distribution from *Hong et al*. [2004]; (*red, RH83*) exponential snow distribution from *Rutledge and Hobbs* [1983]; (*yellow, F07*) moment estimation parameterization from *Field et al.* [2007]; (*purple, R98*) modified exponential snow distribution from *Reisner et al.* [1998]; (*green, H04i*) WDM6 ice distribution from *Hong et al.* [2004].

capabilities of this retrieval algorithm are to be obtained, it is important to maintain differences in ice microphysics between the way the synthetic T_bs are generated and the way they are retrieved. The range in T_bs that results from these differing assumptions should represent a realistic uncertainty estimate.

Because ice particle sizes in the true atmosphere exist on a spectrum, with no clear-cut "ice" and "snow" categories, and because the total integrated amount of cloud ice is retrieved as a single parameter within the 1DVAR framework, a single PSD is used to represent all ice particles in the forward model. The PSD chosen comes from *Field et al.* [2007], hereafter F07. The F07 PSD parameterization is derived from aircraft measurements of frozen PSDs in both tropical anvils and cirrus clouds as well as midlatitude stratiform clouds. An exponential distribution to represent the small end of the size spectrum is combined with a gamma distribution to represent the large end of the spectrum, which allows for the realistic characterization of the narrow peak in particle concentration that is often observed for small ice particles. The F07 parameterization also accounts for the temperature dependency of observed PSDs. Using moment conversions, the F07 scheme allows for a full PSD to be obtained if any moment of the PSD is known. For the purposes of the forward model, the moment used is the one defined by the layer ice water content (IWC, units g/m^3).

In order to convert the IWC and temperature into a full PSD, a mass-diameter relationship for the frozen hydrometeors must be defined:

$$m(D) = aD^b \tag{2.15}$$

where $m(D)$ is the mass for particle with maximum dimension D and a and b are coefficients. The resulting F07 PSD will depend on the choice of a and b. For the forward model, a is chosen to be 52.4 kg/m^3 and b as 3.0, thus assuming the frozen hydrometeors have a constant density of 100 kg/m^3. Noting the definition of IWC,

$$IWC = \int m(D)N(D)dD \tag{2.16}$$

and combining equations 2.15 and 2.16 it can be seen that the b moment of the PSD is given by

$$\mathcal{M}_b = \frac{IWC}{a}. \tag{2.17}$$

Next, following F07, a parameterization is used to relate any moment $\mathcal{M}_n$ (in this case, $\mathcal{M}_b$) to the second moment of the PSD:

$$\mathcal{M}_n = A(n)\exp\,[B(n)T_C]\mathcal{M}_2^{C(n)} \tag{2.18}$$

where T_C is the temperature in degrees Celsius, and $A(n)$, $B(n)$, and $C(n)$ are quadratic functions of n. Equation 2.18 is general and can be used to estimate any moment of the PSD once $\mathcal{M}_b$ has been calculated. In the forward model, with $b = 3$, $\mathcal{M}_3$ is calculated using equation 2.17 and then $\mathcal{M}_2$ from equation 2.18. Once these two moments are known, the full PSD $N(D)$ can be estimated by re-scaling an underlying distribution Φ that is determined by the physics that control the PSD evolution [*Lee et al.*, 2004; *Field et al.*, 2005]:

$$N(D) = \Phi_{23}(x)\frac{\mathcal{M}_2^4}{\mathcal{M}_3^3}, \quad x = D\frac{\mathcal{M}_2}{\mathcal{M}_3} \tag{2.19}$$

Example F07 mass-weighted PSDs (that is, the number concentration times the mass of a particle of a given size; units kg/m^4) for varying values of IWC and temperature are shown in Figure 2.3, along with the corresponding distributions obtained using the snow PSD scheme in WDM6. The F07 parameterization produces a broader distribution with a greater sensitivity to temperature.

As for particle habit, the forward model assumes 6-bullet rosettes (*Liu* shape number 8) for particles with a maximum dimension less than 800 μm and aggregates of 400 μm rosettes (*Liu* shape 12) for particles 800 μm or larger. The forward model is physically realistic, at least, in that smaller rosettes combine to form larger aggregate particles. Thus, the forward model both assumes different particle habits and different PSDs (along with assuming a fixed fraction of frozen particles in each layer) from the radiative transfer model used to generate the synthetic TEMPEST brightness temperatures. The magnitude of the errors created by these differing assumptions is explored further in Chapter 4, but is in line with the spread seen in Figures 2.1 and 2.2. Thus, the forward model error associated with ice microphysics in this experiment is expected to be broadly consistent with what should be expected once actual TEMPEST-D measurements are being conducted. Using a combination of different crystal habits and/or modifying the assumed mass-diameter relationship could potentially improve retrieval performance, and once actual data is available such tuning might be useful. However, to try to do so for the purposes of evaluating the retrieval capabilities on synthetic data would probably not be particularly useful.

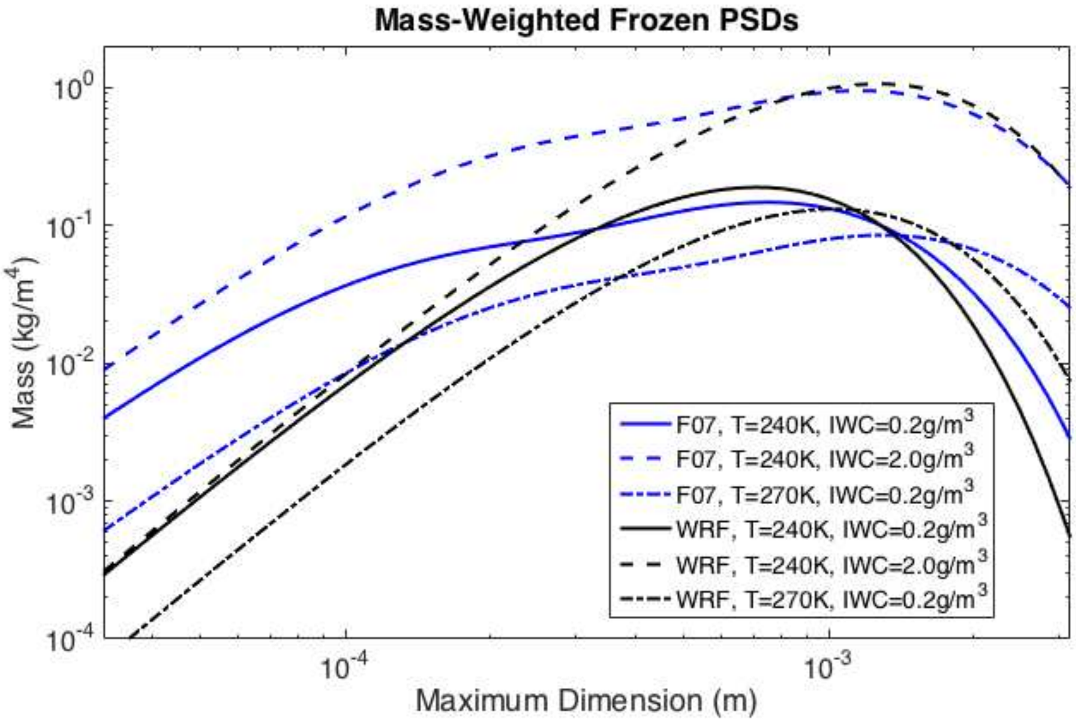

Figure 2.3. Mass distributions for the *Field et al.* [2007] and WDM6 snow PSD schemes, at a temperature of either 240 or 270 K and an ice water content of either 0.2 or 2.0 g/m^3.

2.4.2 Water Vapor Principal Components

While the forward model requires vapor pressure for all 16 vertical levels, it is not feasible to reliably and independently retrieve a full 16-level water vapor profile from only 5 radiometer channels. Thus, to reduce the dimensionality of the problem, 3 principal components of the water vapor profile are retrieved instead. This approach makes use of the fact that water vapor profiles tend to have similar shapes and that the water vapor content of one atmospheric level will tend to be correlated with the water vapor content of the levels above and below it, and follows the example of other retrieval algorithms such as *Boukabara et al.* [2011]. The PCs are defined as variations about a mean profile. For the synthetic retrievals for Hurricane Gonzalo that will be shown, the mean profile and principal components are calculated using all profiles in the simulation at hourly time steps from 0700 to 1800 UTC. For operational use, the mean profile and PCs will be subset by SST and calculated from ERA5 reanalysis data. Water Vapor PCs are calculated in terms of mixing ratio and then translated to vapor pressure as part of the forward modeling process.

The 1DVAR algorithm solves for the coefficient of each PC that results in a minimized cost function (eqn. 2.12). The resulting water vapor profile will be of the following form:

$$\boldsymbol{WV_{ret}} = \overline{\boldsymbol{WV}} + c_1\boldsymbol{PC_1} + c_2\boldsymbol{PC_2} + c_3\boldsymbol{PC_3} \tag{2.20}$$

where $\boldsymbol{WV_{ret}}$ is the retrieved water vapor profile, $\overline{\boldsymbol{WV}}$ is the mean water vapor profile, $\boldsymbol{PC_i}$ is the profile of deviations corresponding to the i-th leading PC, and c_i is the coefficient for the i-th PC, which may be positive or negative. When trying to recreate the true water vapor profiles, it is impossible to capture fine details with 3 PCs. Nevertheless, it is possible to capture most of the variability observed in water vapor profiles. For the WRF model data used in this study, the 3 leading PCs are able to account for 68.2%, 15.9%, and 7.1% of the total variance, respectively. Adding additional PCs gives greatly diminishing returns. Figure 2.4 shows the mean water vapor profile as well as the first 3 principal components. Also shown is a sample water vapor profile, and the fits to that profile that can be obtained using 2 or 3 principal components. This particular profile has an unusually deep layer of moisture near the surface, which is unable to be captured even when 3 PCs are used. Still, the PC representations are far superior to just assuming the mean profile.

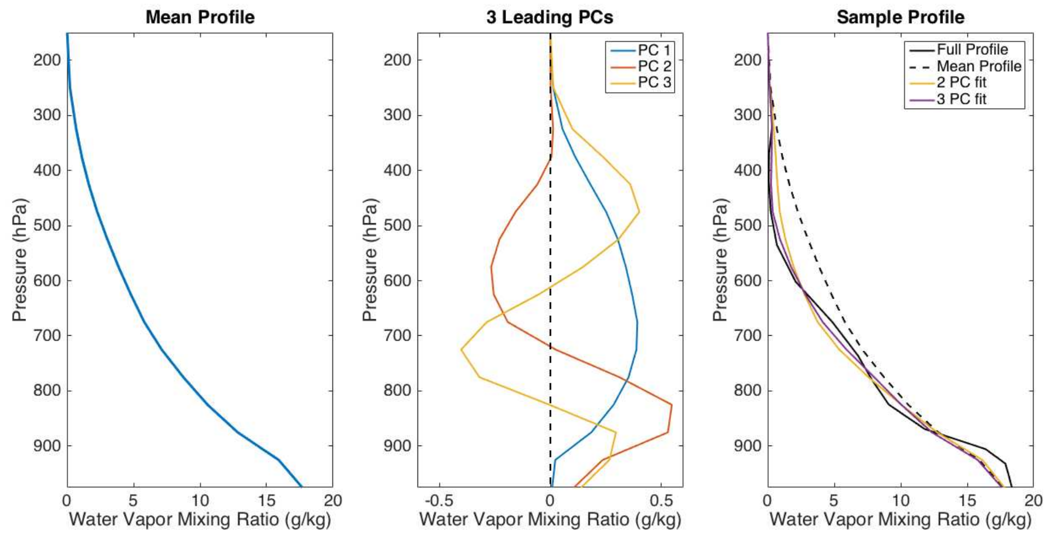

Figure 2.4. *Left:* Mean water vapor mixing ratio profile calculated from the WRF simulation. *Middle*: The departures from the mean profile described by the 3 leading principal components. *Right*: A sample water vapor profile taken directly from the WRF output (solid black), compared to the mean profile (dashed black), and the best-fit profiles that can be obtained using 2 (yellow) or 3 (purple) principal components. The coefficients used are $c_1 = -4.53$, $c_2 = 1.41$, and $c_3 = -1.32$.

2.4.3 Error Covariance Matrices

The matrices $\boldsymbol{S_a}$ and $\boldsymbol{S_y}$ are quite important in guiding the 1DVAR retrieval to a solution. The elements of $\boldsymbol{S_a}$ help determine how much leeway is allowed when finding a solution for the state vector: if the assumed errors are small, the state vector will be forced to be more similar to the a-priori state vector. The $\boldsymbol{S_y}$ matrix determines how much weight each channel is given in the inversion. Channels whose errors are assumed to be smaller are given more weight, with the simulated T_bs at these channels forced to match observations more closely. Determining the right values for $\boldsymbol{S_a}$ and $\boldsymbol{S_y}$ can be a delicate task. In both cases, if the values chosen are too loose, the accuracy of the retrieval will degrade. On the other hand, if the assumed errors are too strict, convergence to an optimal solution will occur less often and it will be harder to draw conclusions from the retrieved parameters.

In this study, the values chosen for $\boldsymbol{S_a}$ come directly from a comparison between the statistics of the WRF model output on which the synthetic retrieval is performed and the ERA5 reanalysis data that is used as a-priori information. This ensures that the assumed a-priori errors are appropriate. The same subset (1/20th of the full model run) is used for calculating $\boldsymbol{S_a}$ as for calculating the water vapor PCs; that is, hourly output from 0700 to 1800. All of the pixels from these files are used to calculate the variance in the difference between the state vector parameters ($\log_{10}$(LWP), $\log_{10}$(IWP), and the coefficients of the water vapor PCs) in the WRF model output compared to the values of those same parameters in ERA5 . These variances make up the main diagonal elements of the matrix. Covariances between the parameters are also calculated and included in the matrix as the off-diagonal elements. Note, however, that the PCs are by definition uncorrelated with each other, so the covariance between PCs is zero.

Determination of $\boldsymbol{S_y}$ is a multi-step process designed to take into account sensor noise, errors in $\boldsymbol{b}$ (the fixed atmospheric parameters assumed by the forward model), and errors introduced by the forward model itself because of its simplified representation of the atmosphere. Since the same emissivity and atmospheric absorption models used by the forward model are used when creating the synthetic TEMPEST brightness temperatures, errors in these compared to the real atmosphere do not contribute to $\boldsymbol{S_y}$, but will be an additional source of error when running retrievals using real TEMPEST-D observations.

Once again, hourly output from the WRF simulation of Hurricane Gonzalo is used to create $\boldsymbol{S_y}$. First, the full atmospheric profiles from the model are converted to the simplified form used by the forward model. The 30 vertical levels in sigma coordinates from WRF are interpolated to yield the 16 fixed pressure levels expected by the forward model. After interpolation, the water vapor profile is further simplified to the profile that can best match the model profile using only 3 PCs. Finally, all of the cloud water from the model profile is summed up and re-distributed evenly between the 800 and 900 hPa pressure levels. Similarly, all of the ice and snow in the model is distributed among the vertical levels as specified by the forward model.

Next, the other atmospheric parameters required by the forward model (namely, wind speed, surface pressure, SST, and the height and temperature profiles) are taken from ERA5. The simplified atmospheric profiles are then run through the same plane-parallel forward model used by the retrieval algorithm and simulated T_bs are calculated. These simulated T_bs are then subtracted from the synthetic TEMPEST T_bs calculated from the full WRF profiles. From this, the variance in T_b differences at each TEMPEST channel is computed. The variances are added to the NEDT values for the channels (to account for sensor noise, which is independent of forward model error) to yield the diagonal $\boldsymbol{S_y}$ elements. The covariances between the errors in each of the channels are also calculated and make up the off-diagonal elements. It should be noted that many 1DVAR microwave retrievals [e.g. *Elsaesser and Kummerow*, 2008; *Boukabara et al.*, 2011] do not include any off-diagonal elements. This decreases computational cost but implicitly assumes no correlation between channel errors, which is probably not a valid assumption. For example, if errors in the forward model create T_b errors at 182 GHz, then it is likely that similar errors will occur at 180 GHz, which lies near the same water vapor absorption line. *Duncan and Kummerow* [2016] showed that the inclusion of error covariances increases skill in cloudy areas, and for this reason the covariances are included in $\boldsymbol{S_y}$.

2.4.3.1 ANGLE DEPENDENCE OF $\boldsymbol{S_y}$

Duncan and Kummerow [2016] applied the CSU 1DVAR algorithm to conically-scanning instruments, with separate $\boldsymbol{S_y}$ matrices for each instrument (because the instruments have different channel configurations) but with the same $\boldsymbol{S_y}$ being used for all retrievals made for each instrument. However, for a cross-track scanning instrument such as TEMPEST, the view angle changes with each pixel in a scan. The change in view angle can affect forward model errors. For example, the higher the view angle, the more significant the errors caused by the plane-parallel assumption become. At nadir, the TEMPEST radiometer sees only the atmospheric profile directly above a given pixel, but at a $45°$ view angle the path of the radiation through the atmosphere will include parts of the atmospheric profile above several pixels. If the surrounding pixels have atmospheric profiles different from the profile corresponding to the surface footprint of the radiometer (invalidating the plane-parallel assumption), then errors in retrieved parameters can result. In addition, the atmospheric path length increases as view angle increases, which can amplify forward model errors. To account for these issues, the process of creating the $\boldsymbol{S_y}$ matrix outlined above is repeated for view angles ranging from nadir to $45°$ in five degree increments, with a separate $\boldsymbol{S_y}$ computed for each view angle. The differences can be considerable; Figure 2.4 shows the difference between the $\boldsymbol{S_y}$ computed at nadir and $45°$. For most channels, the errors are larger at higher view angles; the exception is at 89 GHz. This is likely because this channel is most sensitive to the surface. At nadir, the fact that the atmospheric path length is shorter means that more of the radiation reaching the satellite comes from the surface. Thus errors in assumed surface parameters translate to larger 89 GHz T_b errors at nadir. When performing retrievals, the $\boldsymbol{S_y}$ matrix corresponding to the closest view angle is used.

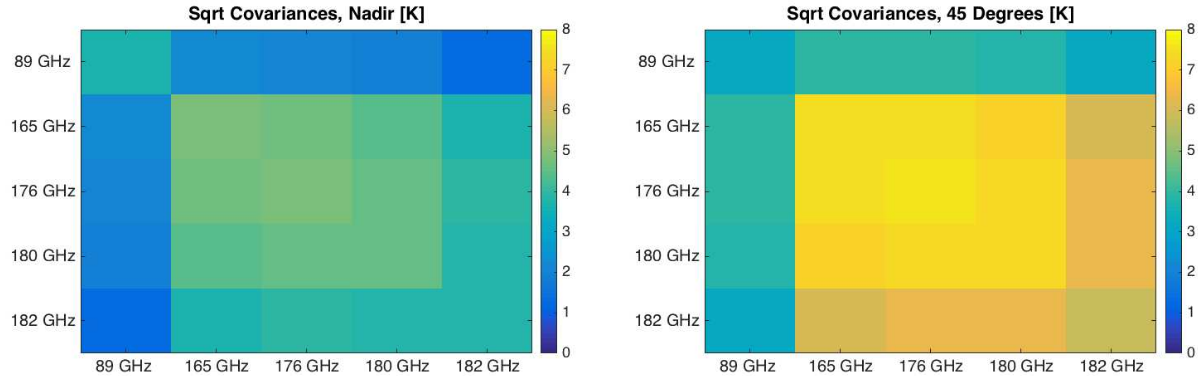

Figure 2.5. Channel error covariance matrix ($\boldsymbol{S_y}$), at both nadir (left) and a view angle of 45° (right). The values correspond to the square root of the covariance between the channels.

2.5 Method of Evaluating Retrieval Performance

The synthetic TEMPEST T_bs generated by the radiative transfer model described in Section 2.3 are input into the 1DVAR retrieval algorithm, with ancillary atmospheric parameters as well as a-priori state vectors for LWP, IWP, and the water vapor PCs taken from ERA5. While the synthetic T_bs are produced on a 3km x 3km grid, the spatial difference between TEMPEST pixels, while dependent on the integration time, will almost certainly be greater than 3 km. If there are 90 pixels per scan, as is the case for the similar MHS, and the altitude of the satellite is 400 km, that would imply a distance between pixels on the order of 10 km. For simplicity, since the WRF model output has 3 km horizontal resolution, comparisons between "true" (WRF model) parameters and the retrieved parameters are done at 9 km resolution. For a given 9 km by 9 km grid box, the synthetic TEMPEST T_bs (which have been averaged over the view-angle-dependent FOV) from the middle of the 9 corresponding WRF grid boxes are used by the 1DVAR algorithm to retrieve LWP, IWP, and the water vapor profile (in the form of 3 PC coefficients). The water vapor profile is used to calculate the TPW, which is also evaluated against the WRF model values. In the results presented in the next chapter, these retrieved parameters are compared to the values of these same parameters for the same grid box of the

WRF output, after the WRF output has been averaged to 9 km resolution. Note, however, that figures in Chapter 3 that show maps of WRF parameters are plotted at the original 3 km resolution, to illustrate the fact that small-scale atmospheric features are not be able to be explicitly resolved by the retrieval algorithm.

The retrieval algorithm struggles in areas of heavy precipitation, as manifest with pixels that fail to converge or associated χ^2 values (equation 2.13) that are quite high, indicating a poor fit. While this is not unexpected, considering that rain drops and graupel particles can have a strong scattering signal, and that the OE forward model has no way to account for rain or graupel, it does suggest that the retrieval algorithm as currently configured is best suited for the evaluation of cloud processes in non-precipitating or only lightly precipitating clouds. In the assessment of retrieved parameters in the following chapter, only 9 km x 9 km grid boxes with a WRF rain water path (RWP) of less than 200 g/m^2 and a graupel water path (GWP) of less than 25 g/m^2 are included in the analysis. These thresholds are chosen somewhat arbitrarily, although the lower threshold for GWP reflects the fact that graupel particles affect T_bs more strongly than an equivalent mass of raindrops.

CHAPTER 3: RESULTS FROM SYNTHETIC TEMPEST RETRIEVALS

3.1 Retrieval Accuracy

Before assessing the consistency of the TEMPEST retrieval algorithm across different view angles, it is helpful to get a sense of the overall accuracy of the retrievals and the limitations of the algorithm. Figure 3.1 shows how the retrieved values of LWP and IWP, assuming either a nadir observation or a view angle of 30 degrees, compare to the actual values in the WRF model, for one time step in the Hurricane Gonzalo simulation. Also shown are the corresponding values from ERA5, which are used as the a-priori values by the 1DVAR algorithm. The algorithm generally retrieves cloud liquid and water in the correct places, although there are some spurious signals in clear-sky areas, and some areas of low ice water path are missed. For the most part, retrieved parameters that result from assuming a nadir observation are best able to match the WRF model output. This is not surprising, given that the FOV is smallest at nadir and that the path of radiation through the atmosphere is the shortest, with less amplification of forward model errors.

Of course, Figure 3.1 shows only one snapshot in time; it is also informative to consider the retrieval performance at nadir across all time steps in the simulation. To this end, Figure 3.2 shows density plots comparing retrieved values of TPW, LWP, and IWP with the WRF model values, and Table 3.1 gives error statistics for the both the retrieved values and the values taken from ERA5. The table is split into clear sky and cloudy sky pixels because the errors in the retrieval are of a somewhat different nature in these two regimes.

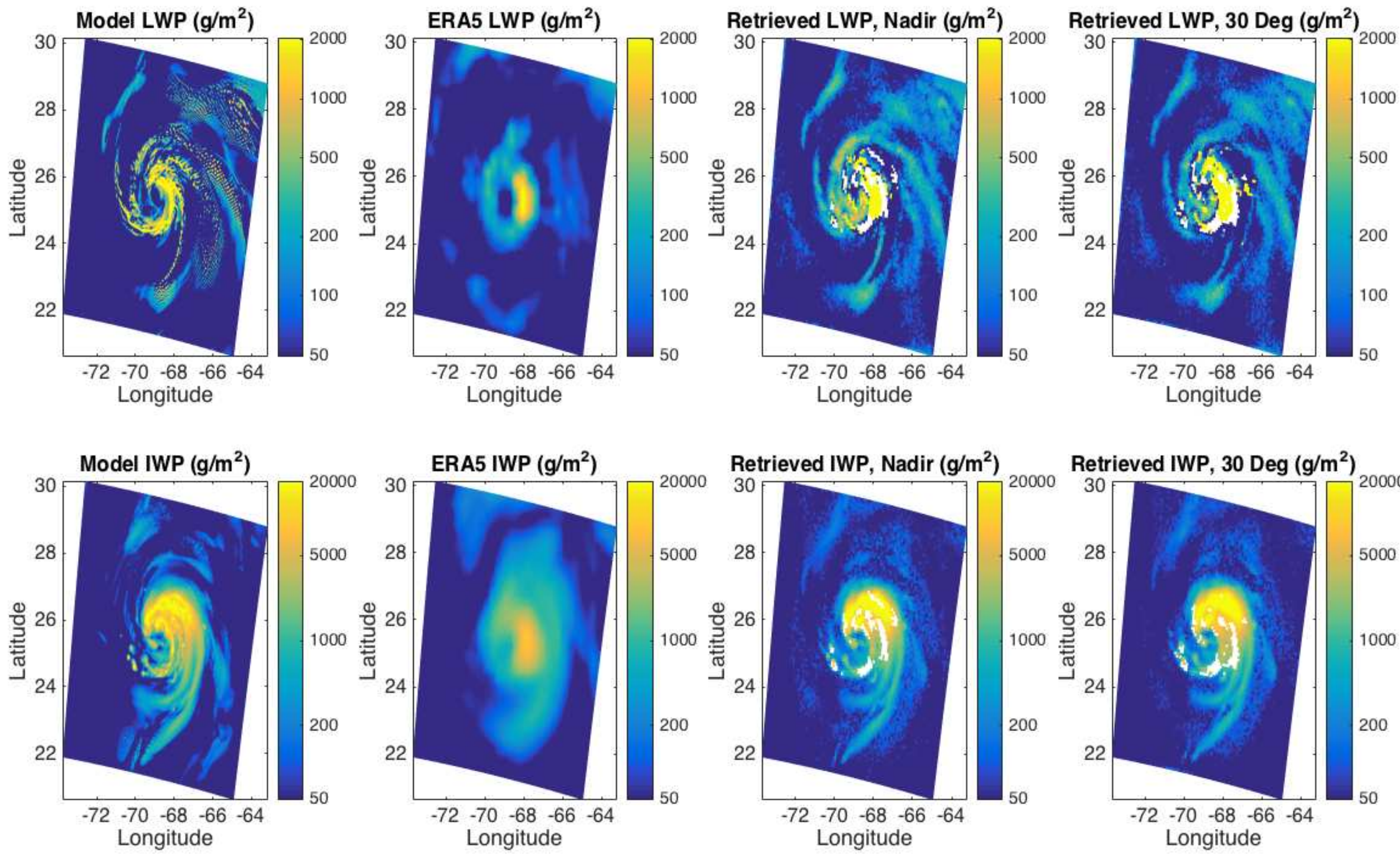

Figure 3.1. Liquid water path (top row) and ice water path (bottom row) at 1000 UTC in grams per square meter, taken from the WRF simulation (left column) and ERA5 reanalysis (second-from-left column). The rightmost columns show the same scene as retrieved by the 1DVAR algorithm at nadir and at a view angle of 30 degrees.

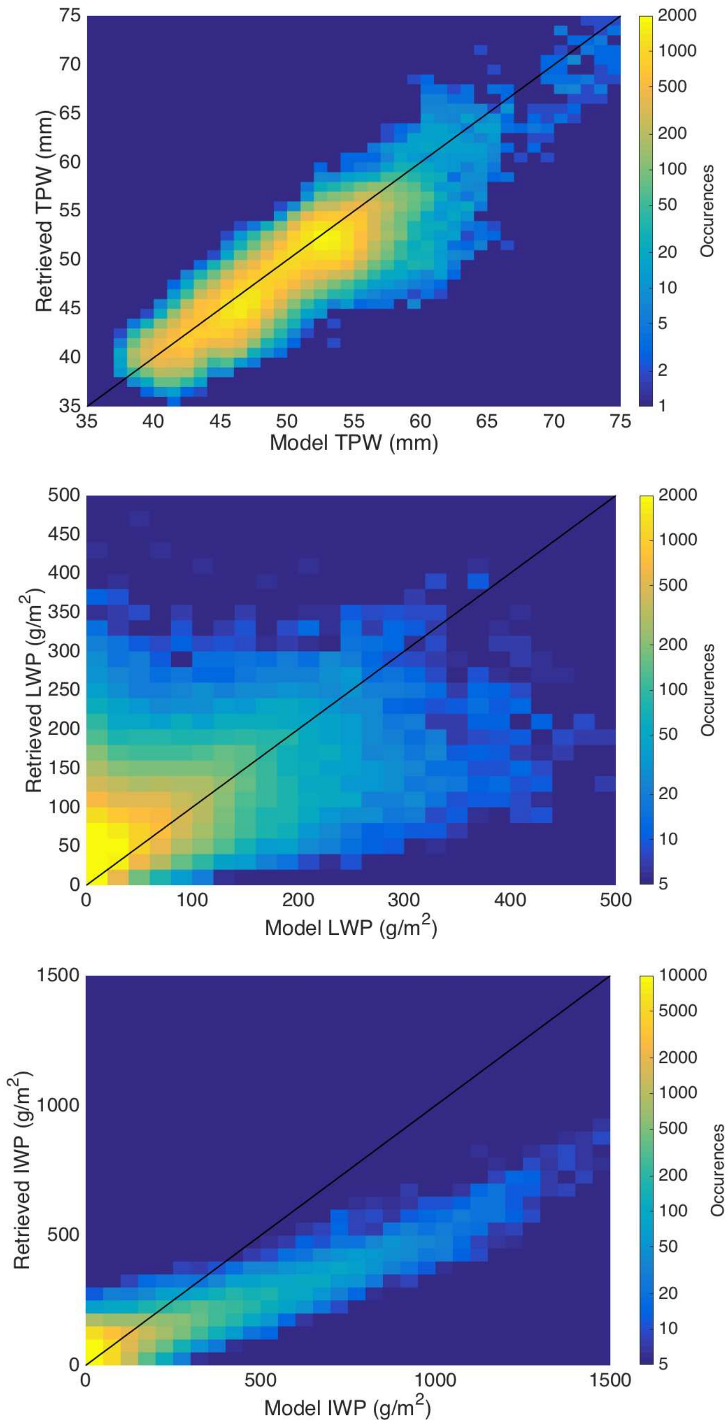

Figure 3.2. 2-D histogram of retrieved parameters (ordinate) compared to the actual parameters from the WRF model run used to generate the synthetic TEMPEST observations (abscissa). The solid black line in each panel represents the one-to-one line.

Table 3.1 Correlation, bias, and root-mean-square error (RMSE) for the retrieved values of TPW, LWP, and IWP, as well as the corresponding error statistics for the ERA5 interim data that is used as a-priori information for the retrieval. Statistics are shown for both clear-sky (IWP < 10 g/m^2, LWP < 10 g/m^2; 36,864 pixels total) and cloudy regimes (LWP > 50 g/m^2 or IWP > 50 g/m^2; 37,739 total pixels). LWP and IWP correlations are not included for the clear-sky regime because by definition the correlation between any collection of non-zero values and a collection of zeros (the true value of LWP or IWP when there is no cloud) is zero.

Clear Pixels (n=36864)						
	Retrieval Correlation	Retrieval Bias	Retrieval RMSE	ERA5 Correlation	ERA5 Bias	ERA5 RMSE
TPW	0.883	-0.79 mm	2.30 mm	0.857	-1.07 mm	2.59 mm
LWP	-	+28.8 g/m^2	43.2 g/m^2	-	+44.1 g/m^2	58.7 g/m^2
IWP	-	+21.8 g/m^2	36.7 g/m^2	-	+56.7 g/m^2	266.1 g/m^2
Cloudy Pixels (n=37739)						
	Retrieval Correlation	Retrieval Bias	Retrieval RMSE	ERA5 Correlation	ERA5 Bias	ERA5 RMSE
TPW	0.839	-1.37 mm	2.89 mm	0.858	-1.46 mm	2.83 mm
LWP	0.457	+5.5 g/m^2	214.1 g/m^2	0.038	-31.6 g/m^2	234.7 g/m^2
IWP	0.915	-64.6 g/m^2	158.8 g/m^2	0.363	+250.9 g/m^2	922.5 g/m^2

In clear-sky conditions, the retrieval shows moderate skill at retrieving TPW, with a correlation coefficient (0.883) that is slightly higher than the correlation with a-priori values. The negative bias is also reduced, and the root-mean-square error (RMSE) is lower as well. On the other hand, in cloudy conditions, the retrieved TPW values are, on average, not much better or worse than the a-priori ERA5 values, indicating that the radiometric signals of cloud water and cloud ice tend to mask the more subtle signatures of the water vapor PC coefficients.

For the purposes of observing cloud processes, of course, what is more important is the accuracy of the retrieved values of LWP and IWP. Both parameters tend to be overestimated in clear-sky and even light-cloud regions. Some of this bias is inevitable. The nature of the distribution of cloud water and cloud ice means that there are many cloud-free pixels, and radiometric noise as well as forward model errors can, in some cases, lead to T_bs that are best matched by the inclusion of a small amount of cloud water or cloud ice. Since negative values of cloud water and cloud ice are not allowed in the forward model, this will lead to a positive bias in retrieved LWP and IWP. Additionally, brightness temperatures in clear-sky areas that are adjacent to clouds will be affected by the clouds, since the TEMPEST FOV is larger than 9 km. This also contributes to the positive bias. Thus, small retrieved values of LWP and IWP (below about 50 g/m^2 or so) should be treated with skepticism, and the retrieval algorithm should not be considered to be especially sensitive to thin clouds.

At higher cloud amounts, the retrieval shows skill in retrieving both LWP and IWP. The correlation coefficient for both parameters is much higher than in the a-priori data, with reduced biases and RMS errors as well. The retrieval is less sensitive to cloud water than it is to ice, with a considerably lower correlation coefficient and a density plot in Figure 3.2 that shows considerably more scatter (it should be noted, however, the logarithmic color scale somewhat exaggerates this scatter). LWP tends to be underestimated for high LWP amounts in WRF. This is due to several factors, which are explored more fully in Chapter 4.

On the other hand, retrieved IWP has a very high correlation with model IWP; however it is consistently underestimated. This is readily apparent from the density plot in Figure 3.2, where the slope of the distribution is much less than 1. This bias stems mostly from the differences in ice mircophysics (habit and PSD) between the forward model and the radiative transfer model used to generate the synthetic brightness temperatures. Using the WRF microphysics leads to smaller particles, on average, which have less of an effect on T_bs than ice in the forward model, and so the retrieval settles on a smaller total amount of ice to best match the observed T_bs. As explained in Section 2.4.1, these differences are presumed to be representative of the true uncertainties in our current understanding of real-world ice microphysics. This result also suggests that the retrieval is not particularly sensitive to small ice particles, while giving a more reliable estimate of the amount of larger "snow" particles. Importantly, however, the very high correlation means that the retrieval is very good at determining where there is *more or less ice*, and this is critical for observing changes in cloud ice over time, even if fundamental uncertainties in ice microphysics preclude high-accuracy measurements of the total IWP.

3.2 Observing Rapidly-Changing Cloud Characteristics

For a proposed TEMPEST constellation of CubeSats, even more important than the overall accuracy of the retrieved parameters is the consistency of the parameters – are differences caused by making retrievals at different view angles small enough that true changes in atmospheric parameters can be discerned? While this question is addressed from a more statistical point of view in Section 3.3, here, we shall gain insight into the problem through a more detailed analysis of three, 30-minute long case studies from the WRF model run, in which cloud fields are rapidly changing over a limited domain. 30 minutes is used because it represents the outer limit to the period of time over which the same cloud feature could be observed from a TEMPEST-type cluster of satellites in the same orbit, at least over the tropical oceans. The surface of the earth (at the equator) moves at a speed of 460 meters per second; thus in 15 minutes it will have moved about 414 km. The distance between the sub-satellite point and the edge of the TEMPEST swath is also a little over 400 km. If a point were directly under a TEMPEST satellite at t=0, then at t=-15 minutes that same point would have been located on one edge of the swath and at t=15 minutes on the other edge of the swath.

First, let us consider a cirrus cloud shield in a region to the southeast of the core of the hurricane that dissipates between 0800 and 0830 UTC. Figure 3.3 shows the change in the IWP in the WRF simulation over this period, as well as retrieved IWP for each snapshot calculated at

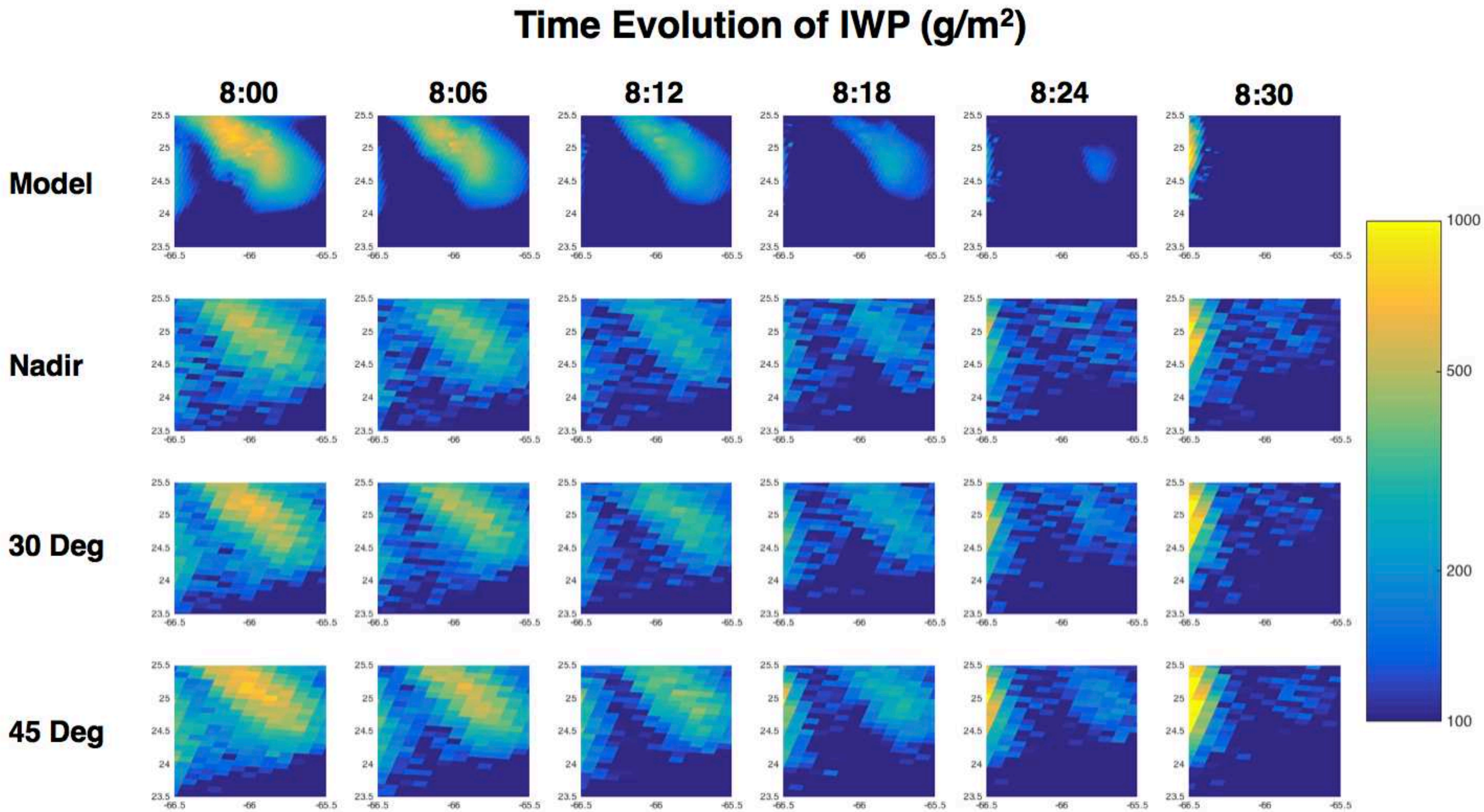

Figure 3.3. The top row of plots shows IWP from the WRF Hurricane Gonzalo simulation between (66.5° W, 23.5° N) and (65.5° W, 25.5° N), at 6-minute increments from 0800 to 0830 UTC. The lower rows show the same scene as retrieved by the 1DVAR algorithm at various view angles.

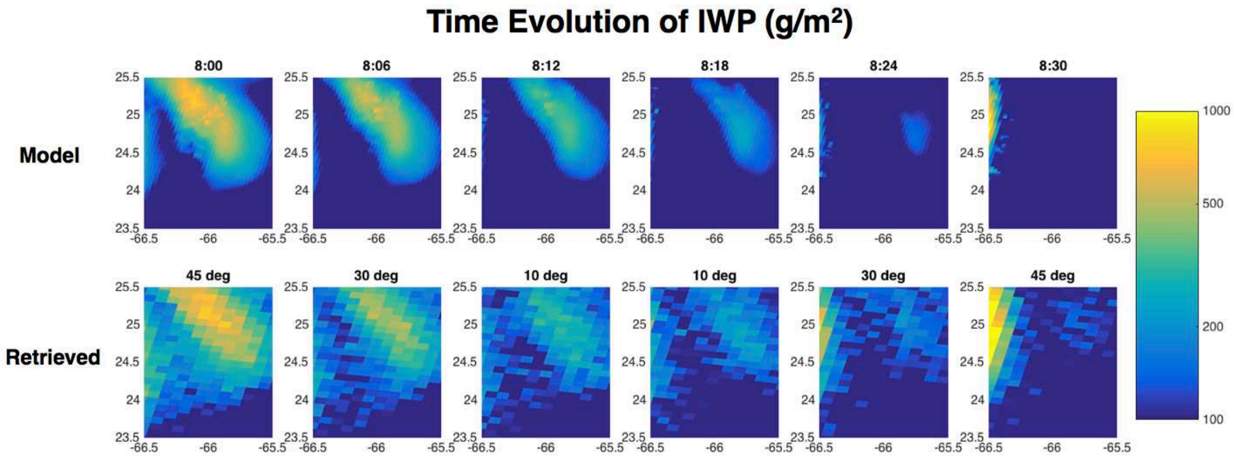

Figure 3.4. As in Fig. 3.3, except only a single series of retrieved IWP values are shown, with a different view angle for each time, mimicking the behavior of a constellation of TEMPEST CubeSats.

view angles of 0, 30, and 45 degrees. The retrieval does not capture the evolution of the IWP field perfectly; low values of IWP are retrieved in some areas that are clear, and the lower spatial resolution of the retrieval means that features tend to blur together. Still, at any given view angle the general decreasing trend in IWP is clear, and the differences due to view angle at any given time are small. These facts suggest that a sequence of satellites, making measurements at different view angles, would be able to faithfully capture the dissipation of the cirrus clouds. This is shown even more clearly is Figure 3.4. Here, the same sequence of snapshots from the model is shown, but it is assumed that a TEMPEST satellite observes the scene with a view angle of negative 45 degrees at 0800 UTC, and then a sequence of TEMPEST satellites go on to observe the same scene at 6 minute intervals thereafter, until finally a last observation is made with a view angle of 45 degrees in the opposite direction. Even with realistically changing view angles, the retrieval clearly captures the dissipation of the cloud field.

When it comes to measuring changes in cloud water, view angle differences can be more problematic. For example, Figure 3.5 shows the rapid development of new, liquid clouds in a band to the south of the center of Gonzalo. At nadir, the retrieval is able to capture the evolution of this cloud system quite well, even if the LWP is underestimated by a bit (since this is a narrow band of clouds, FOV averaging probably contributes to this underestimation, along with the 89 GHz channel saturation that is described in Chapter 4). At higher view angles, however, the accuracy of the retrieval degrades. While at a constant view angle of 30 degrees the general pattern of the cloud development is still apparent, there are significant differences between the retrieved values at 30 degrees and nadir. At 45 degrees, the scene appears totally different. If the retrievals at these different view angles are stitched together to imitate a TEMPEST constellation (middle row of Fig. 3.5), one gets the impression that the cloud amount is lessening, which is of course the opposite of what is happening.

This scene demonstrates a problem that is common for the retrieval at high view angles; namely, the retrieval tends to settle on high and low values of LWP at the expense of moderate values. In some cases, in fact, the retrieval even mistakes areas of high LWP as areas with near-zero LWP. The reason for this is explored more fully in Chapter 4; but, put simply, much of the T_b sensitivity at TEMPEST frequencies is lost at high view angles, especially in areas of high TPW, high winds, or cloud-top pressures that are above the 800 mb assumed by the forward model. The T_b response at 89 GHz saturates, with dramatic changes in LWP leading to only small changes in measured T_bs. The T_b response is also nonlinear and in some cases even non-monotonic. All of this means that the retrieval becomes prone to mistakenly settling on extreme values to minimize differences between observed and forward modeled T_bs.

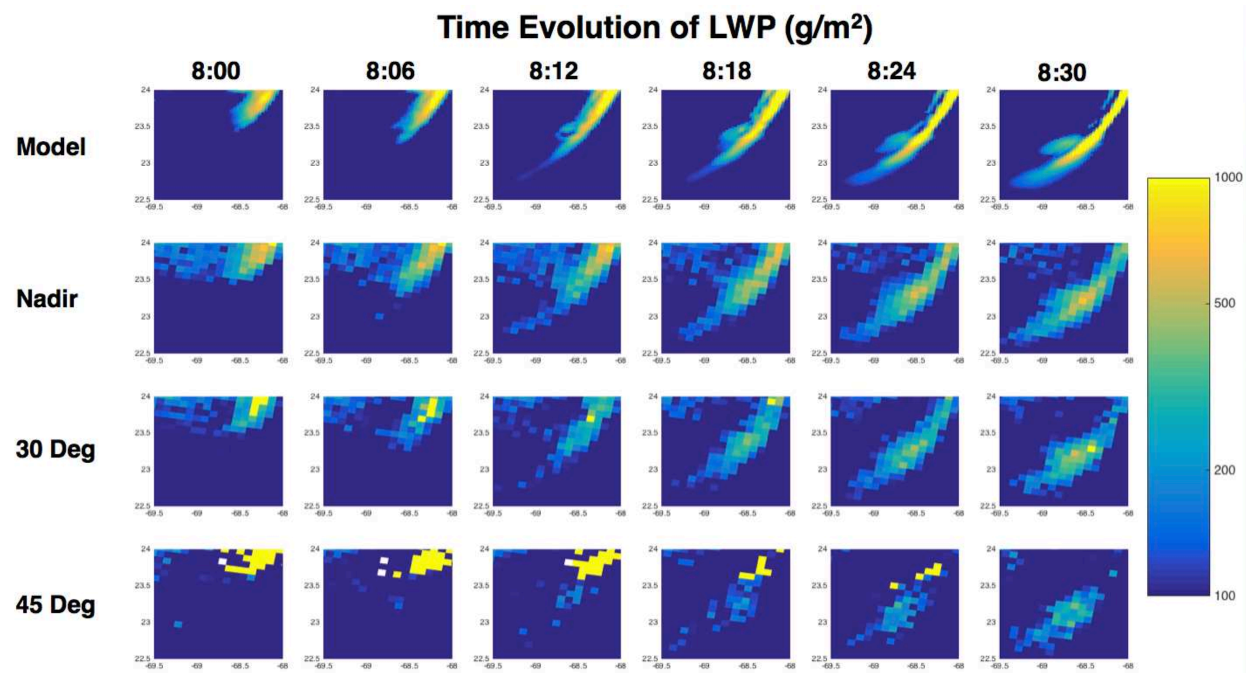

Figure 3.5. As in Fig. 3.3, except LWP is plotted and the domain is the region between (69.5° W, 22.5° N) and (68° W, 24° N).

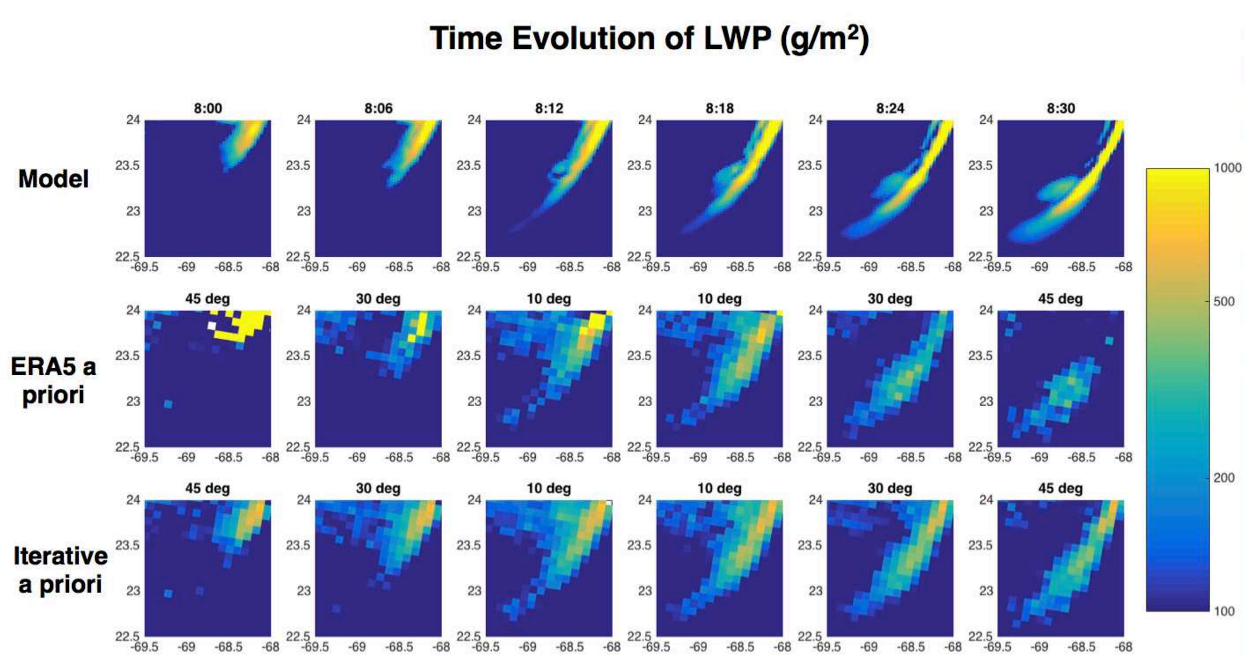

Figure 3.6. *Top row:* WRF simulation LWP field, at 6-minute increments. *Middle*: Scene as viewed from a series of satellites at varying view angles, with the a-priori assumptions about the atmospheric parameters being taken from ERA5 each time. *Bottom*: Retrieved LWP values obtained by using time-adjacent retrieved values as a-priori information, as described in the text.

Thankfully, in the context of a train of satellites, a significant portion of this error can be rectified by making use of the information provided by preceding or subsequent satellite observations. The tendency of the retrieval at high view angles to settle on extreme values can be mitigated by placing more strict limits on the assumed a-priori errors. For a single high-view-angle observation, this can be problematic because reducing the assumed error will make the final retrieved value track more closely with the a-priori value, which might be well off the mark, at least in the case of ERA5 – it is hard to put clouds in exactly the right place. With a cluster of satellites, however, one can leverage the more reliable information that can be obtained by observations closer to nadir.

The way this is done is as follows. For high view angle retrievals, the a-priori values of LWP, IWP, and the 3 water vapor PCs are taken from the time-adjacent overpass of the same pixel by a preceding or subsequent CubeSat. This process is done iteratively; so, for the case shown in Figure 3.6, the retrieval at 10 degrees at 0818 UTC would be used to provide the a-priori values for the retrieval at 30 degrees at 0824 UTC, and the retrieval at -10 degrees at 0812 UTC would be used to provide the a-priori values for the -30 degree retrieval at 0806 UTC. Then the 0824 retrieval would be used as a-priori information for the 0830 retrieval and the 0806 retrieval as the a-priori for the 0800 retrieval. When this is done, the assumed a-priori error variance in the $\boldsymbol{S_a}$ matrix is also reduced to 200 g^2/m^4 for both LWP and IWP. This moderate value allows the retrieved values of LWP and IWP to change in response to clear increases or decreases, but prevents the algorithm from making large changes to these parameters in exchange for only slightly better T_b agreement. The results of using this iterative method are shown in the bottom row of Figure 3.6, and it is clear that this modified retrieval does a much better job of capturing the actual changes in LWP.

This improvement speaks to the value of using an optimal estimation retrieval algorithm as opposed to simply a minimum variance method; that is, one in which the differences between observed and forward modeled brightness temperatures are minimized without any a-priori probability distribution function assumed for the state vector. Because of the weak radiometric response at high view angles, a minimum variance method would not be appropriate, and the weak a-priori constraints provided by ERA5 are insufficient. However, having several TEMPEST instruments provides a wealth of additional, more accurate a-priori information with which to further constrain the state vector.

A downside of this approach is that, while nadir retrievals are generally more reliable than retrievals at higher view angles, if any significant errors in the retrieved values exist at nadir, then these errors can propagate to successive or preceding higher-view-angle retrievals as they become tied to erroneous a-priori assumptions. Still, differences in retrieved values from one TEMPEST overpass to the next should be informative, even if the values themselves are biased low or high because of errors in the nadir retrieval.

Finally, it should be noted that while using low-view-angle retrievals as a-priori information for higher-view-angle retrievals is almost uniformly helpful, it is not a silver bullet to eliminate all problems at high view angles. Figure 3.7 shows another example of a rapidly changing cloud field, this time to the northwest of the storm center between 0918 and 0948 UTC. While at any constant view angle the general trend is clear, much less LWP is retrieved at a 45 degree view angle and this creates a problem when trying to piece together a picture of the cloud development from multiple satellites (Figure 3.8). In this case the negative bias at high view angles is not merely an artifact of a flat T_b response, but rather a radiometric signal at high view angles that the algorithm interprets as a lower LWP. Using the iterative a-priori approach (bottom row) helps somewhat, but there are still lower retrieved LWP values at 0948 UTC compared to 0936 UTC or 0942 UTC, even though the actual model values are increasing.

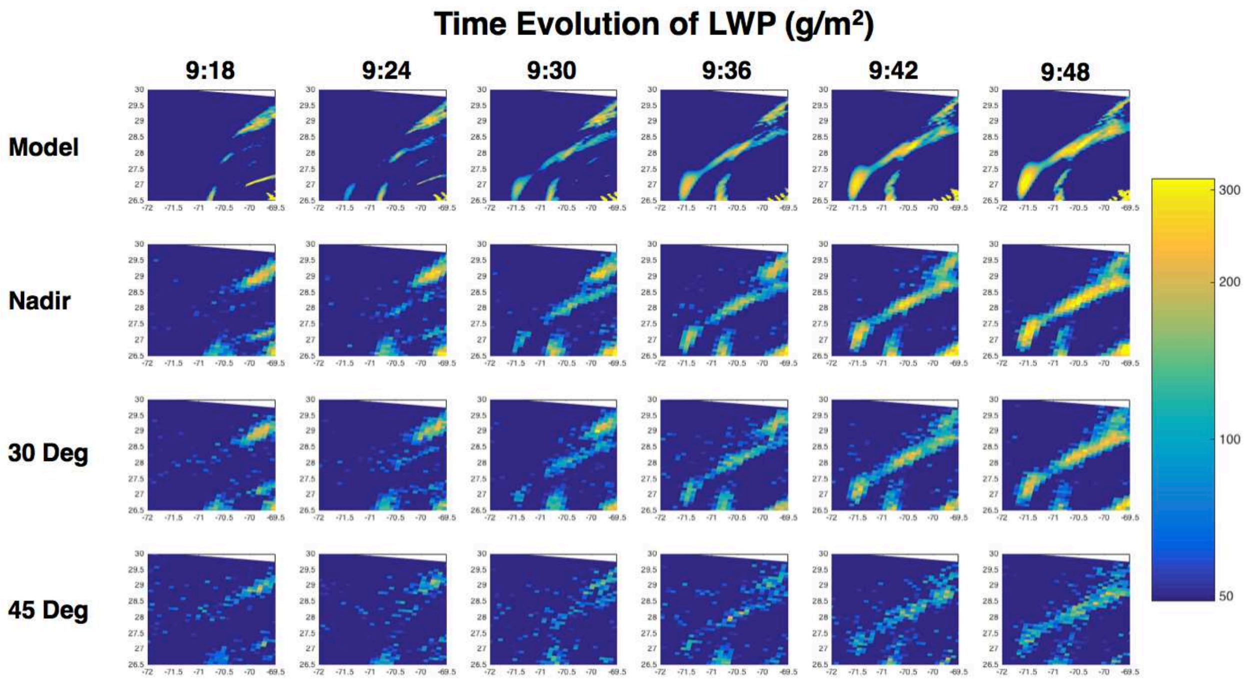

Figure 3.7. As in Figure 3.5, but for the region between (72° W, 26.5° N) and (69.5° W, 30° N) from 0918 UTC to 0948 UTC.

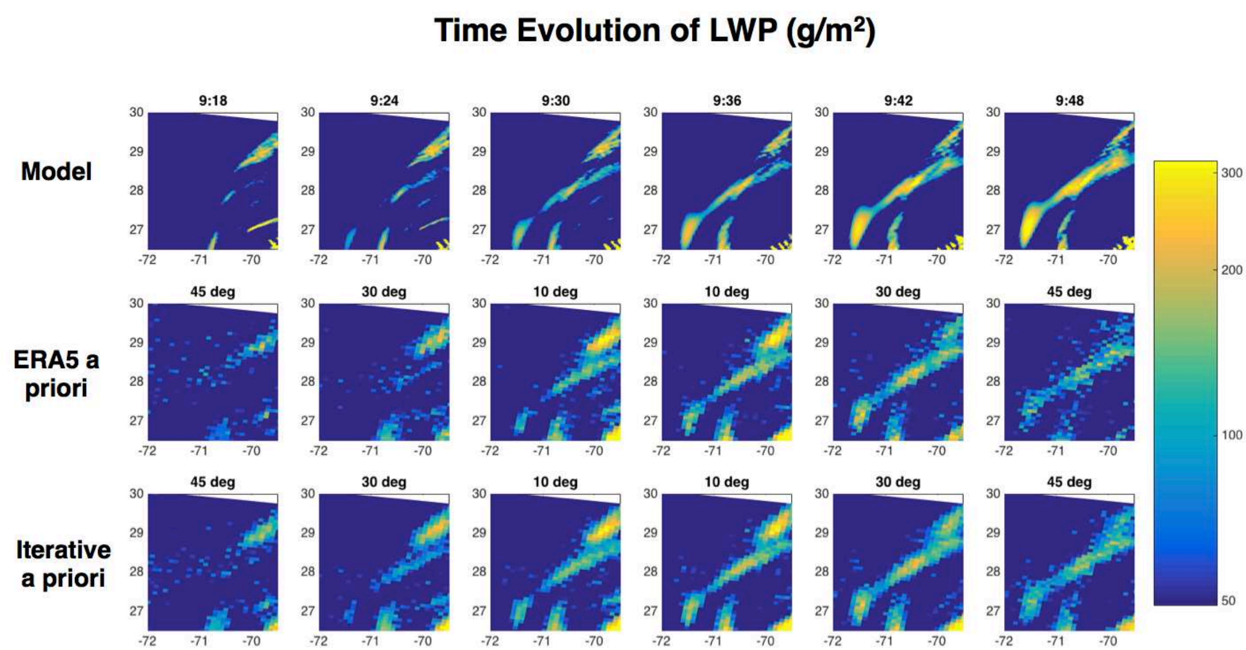

Figure 3.8. As in Figure 3.6, but for the region between (72° W, 26.5° N) and (69.5° W, 30° N) from 0918 UTC to 0948 UTC.

3.3 Statistical Consistency Across View Angles

It is also possible to evaluate the consistency of the retrieval at different view angles by looking at all of the pixels in the simulation collectively. Figure 3.9 shows the values for the same error statistics listed in Table 3.1, but shows how each changes a function of view angle. The statistics shown are calculated using output from the iterative version of the retrieval described in the previous section, and for simplicity all pixels (clear and cloudy sky) are included.

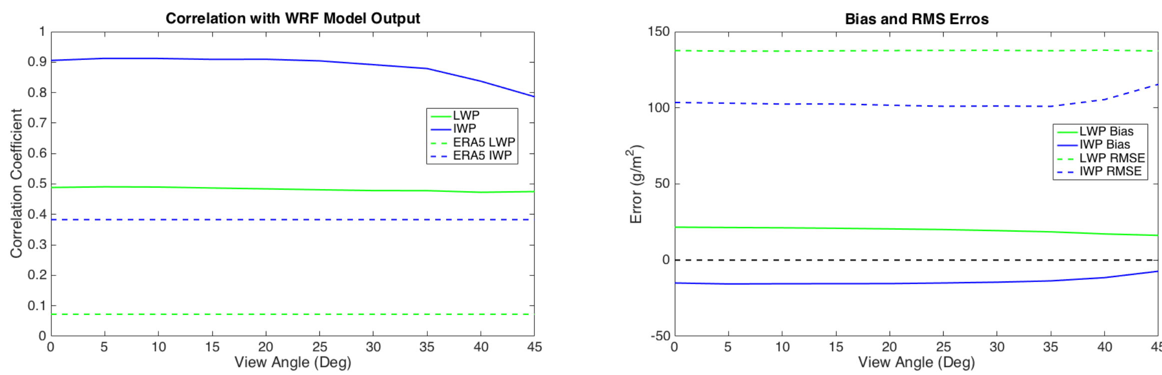

Figure 3.9. *Left*: Correlation coefficient between retrieved and model values of LWP (green) and IWP (blue), for view angles ranging from nadir to 45 degrees. The horizontal dotted lines show the ERA5 correlation values, for comparison. *Right*: Bias and root-mean-squared errors for retrieved LWP and IWP, again as a function of view angle.

As noted in Section 3.1 the correlation coefficients for both LWP and IWP are significantly higher than the correlation with ERA5 data. Figure 3.9 demonstrates, however, that the correlation coefficients are also quite consistent, at least out to a view angle of about 30 or 35 degrees. At this point the correlation coefficient for IWP starts to decrease, and the correlation for LWP also slightly decreases. Similarly, when looking at bias and RMSE, the retrieval is quite consistent up to a view angle of 35 degrees. At the highest view angles, LWP starts to become biased low compared to lower view angles (this effect is evident in the case study presented in

Fig. 3.8), and IWP starts to become biased higher. The RMSE for IWP also increases at high view angles.

Lastly, we can ask the question: how does the distribution of errors caused by viewing a scene from different angles compare to the distribution of differences in LWP and IWP that occur at WRF model grid points at intervals of only a few minutes? If one hopes to reliably retrieve information about changes in the amount of cloud liquid and cloud ice, then that first distribution must be narrower than the second. These distributions, for model output at 1000 UTC, are shown in Figure 3.10. The figure shows results both for retrievals that assume a constant ERA5 grid of a-priori state vectors for all view angles, and for retrievals that make use of lower view angle retrieved values for a-priori information. The figure shows histograms of differences between retrievals at 30 degrees and 10 degrees (corresponding to a temporal difference of close to 6 minutes), as well differences between retrievals at 45 degrees and nadir (associated with about 15 minute spacing). These error distributions are generally within the corresponding model error distributions, calculated by subtracting the model value of LWP/IWP at 1000 UTC from the value of the same pixel at 0954 UTC or 0945 UTC. This is particularly true when the iterative version of the retrieval is used, which narrows both the LWP and IWP error distributions, but particularly the LWP distribution, for the reasons discussed in Section 3.2. It should be noted that some of the differences in the WRF model from one time step to another are simply due to advection, and not meaningful changes in the properties of individual clouds. Still, judging from these distributions, one can infer with reasonable confidence that changes on the order of 50 g/m^2 or larger in retrieved LWP or IWP from one TEMPEST observation to the next likely reflect true changes in the atmosphere, while smaller changes could just be noise.

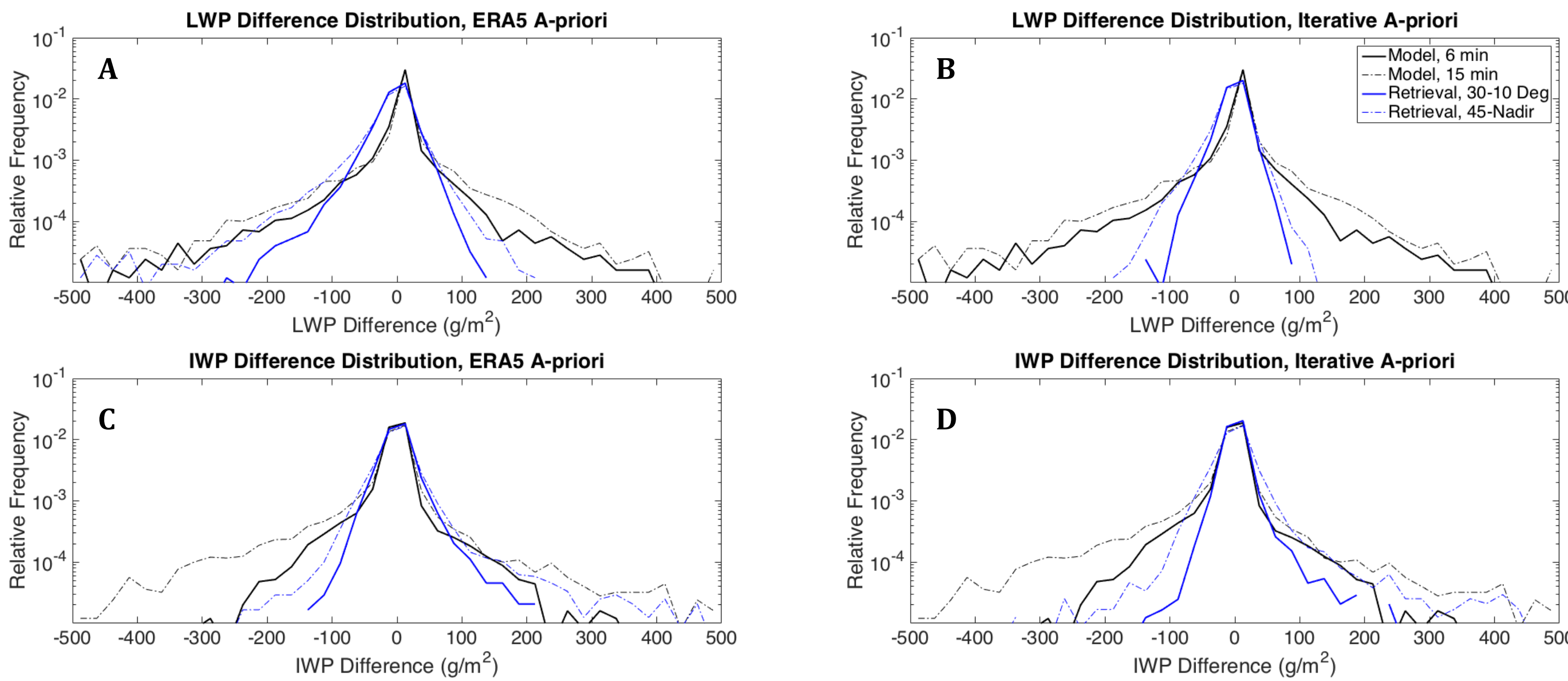

Figure 3.10. (A) Distribution of errors in LWP using ERA5 data as a-priori information at all view angles. (B) Distribution of errors in LWP using the iterative approach to assigning a-priori values described in the text. (C) As in panel A, but for IWP. (D) As in panel B, but for IWP. *All panels*: The blue distributions show the differences in retrieved values for view angle pairs of 30 degrees and 10 degrees (solid line) or 45 degrees and nadir (dotted line). The black distributions shows the differences in model simulation values between 1000 UTC and 0954 UTC (solid line) or 0945 UTC (dotted line).

CHAPTER 4: CHANNEL SENSITIVITIES AND ERROR ANALYSIS

4.1 Channel Sensitivities

In this section we examine the sensitivity of the various TEMPEST channels to changes in the atmospheric parameters retrieved by the 1DVAR algorithm. This leads to a greater understanding of the factors contributing to errors in the retrieved values, and how they change with view angle. Let us begin by considering the weighting functions for the TEMPEST channels under clear-sky conditions. If $\breve{T}_{\lambda}(z)$ is the transmittance of the atmosphere at height z for radiation at wavelength λ, representing the fraction of energy emitted at a given level in the atmosphere that makes it to the top of the atmosphere, then the weighting function for a channel at wavelength λ is given by the derivative $\frac{d\breve{T}_{\lambda}(z)}{dz}$. The weighting function is an indication of where in the atmosphere the radiation at a given channel comes from. The weighting function depends on the atmospheric state, and also depends weakly on view angle. Figure 4.1 shows the weighting functions for a nadir observation at the TEMPEST frequencies for two sample clear-sky pixels from the WRF simulation.

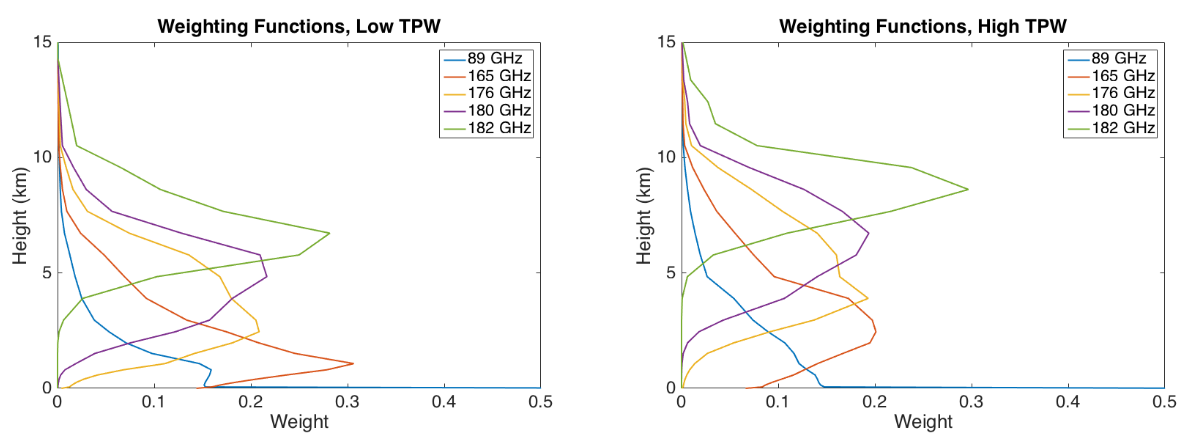

Figure 4.1. *Left*: Weighting functions at nadir for the TEMPEST frequencies for a representative pixel from the WRF simulation with a TPW value of 42.5 mm. *Right*: Weighting functions for a much more moist pixel, with a TPW value of 73.1 mm.

Note that when the atmospheric column is moister, the weighting functions peak higher in the atmosphere. While not shown here, the weighting functions at a higher view angle would also peak higher in the atmosphere, although the effect is less dramatic. Note also that while the 89 GHz channel has a significant sensitivity to the surface, the 165 GHz channel is only slightly sensitive to surface characteristics, and at the other channels all of the radiant energy that reaches the satellite is coming from higher up in the atmosphere.

Keeping the general structure of these weighting functions in mind, let us now consider the sensitivities of each channel to changes in the two retrieved parameters most important for understanding cloud processes, LWP and IWP. To explore these sensitivities, the same sample atmospheric profile described in section 2.4.1 was run through the 1DVAR forward model, with varying amounts of either LWP or IWP (the results for liquid assume no ice, and the results for ice assume no liquid). The effect of these changes on the forward modeled T_bs are shown in Figure 4.2.

It is clear that nearly all of the LWP signal comes from radiances at the 89 GHz channel, as the T_bs are nearly flat at the other frequencies. When there is no liquid water in the column, microwave energy at 89 GHz comes partly from the surface and partly from the atmosphere. As more cloud water is added, the cloud water absorbs and re-emits some of the upwelling energy coming from the surface, meaning that more of the energy that reaches the satellite is coming from the atmosphere rather than the surface. Since the emissivity of the ocean at 89 GHz is significantly less than unity, the atmosphere appears "warmer" than the surface does and thus as LWP increases so does the 89 GHz brightness temperature. Eventually, however, saturation is reached, where the cloud fully masks the surface, and adding more liquid water has little effect on brightness temperatures. This demonstrates why it is hard to make accurate retrievals for high

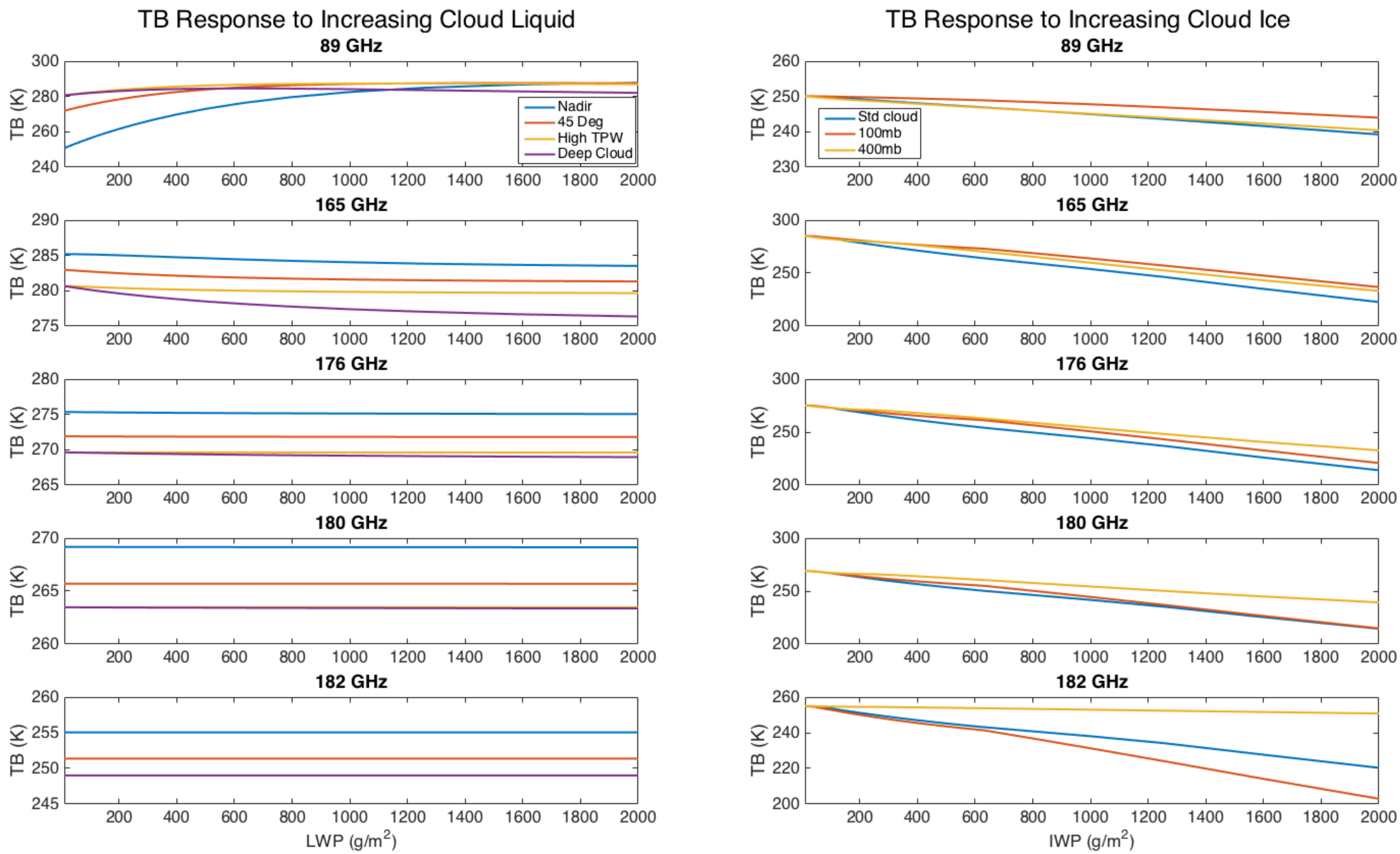

Figure 4.2. *Left:* T_b as a function of LWP at TEMPEST frequencies for retrievals made at nadir (blue), at a view angle of 45 degrees (red), at a 45° view angle plus with 25% more water vapor (yellow), and at a 45° angle, with high TPW and a deeper cloud extending up up to 650 hPa (purple). *Right*: TEMPEST T_bs as a function of IWP using the cloud ice distribution assumed in the forward model (blue), assuming a cloud layer from 100hPa to 200 hPa (red), or assuming a cloud layer from 400 to 500 hPa (yellow).

values of LWP – there simply isn't much of a radiometric signal at the TEMPEST frequencies with which to discern the difference between, say, a LWP of 1000 g/m^2 or 2000 g/m^2. The retrieval will be guided by a-priori information in such cases.

The problem is worse, however, at higher view angles. In this case, the path length through the atmosphere is longer, so the radiometer sees less of the surface to begin with. Thus the contrast in 89 GHz T_bs between a clear scene and a cloudy one is reduced, and the channel becomes saturated at even lower amounts of liquid water. As can be seen in Fig. 4.2, there is very little radiometric signal beyond 500 g/m^2 or so. Other factors that can reduce the LWP signal at 89 GHz include high TPW or high surface wind speeds. As seen from the weighting functions, increasing the amount of water vapor in the atmosphere decreases the surface contribution, and sea surface emissivity increases with increasing wind speed, reducing the contrast between the effective temperatures of the atmosphere and surface.

A final complication is that, while the forward model assumes a cloud layer extending from 800-900 hPa, cloud water can exist above this level. In this case, the trend in 89 GHz temperature with increasing LWP can actually reverse itself, with 89 GHz T_bs being lower at high amounts of LWP than at medium amounts (because the effective emission temperature of the cloud is lower). Because the forward model assumes a constant cloud top at 800 hPa, it is unable to recreate this decrease in T_b with increasing LWP and thus instead takes cloud liquid away to try to match the observed 89 GHz T_b. While a deep liquid cloud layer like this does create a radiometric signal at 165 GHz, the forward model cannot recognize it if the cloud height is assumed to be fixed. The issues raised above all point to sources of error in the retrieval of LWP, and help explain why it is so important to constrain the a-priori LWP information used when trying to retrieve at a high view angle.

In contrast to IWP, Figure 4.2 shows that LWP has a clear, relatively linear radiometric signal at all TEMPEST frequencies, although the response is much more muted at 89 GHz. The vertical placement of the cloud ice, however, can have important consequences, especially at the 182 GHz channel. Because the weighting function at 182 GHz peaks high in the atmosphere, if most of the ice mass is below the peak in the weighting function, then most of the ice scattering signal at 182 GHz will be lost, even though a strong scattering signal will still be present at other channels. This can confuse the retrieval algorithm, causing errors in the retrieved IWP due to the uncertainty in the proper vertical placement.

4.2 Error Analysis

A series of experiments was performed to quantify the effect of the various assumptions that combine to make up the forward model error. Using the forward model, and all of the simplifications contained therein, TEMPEST T_bs were calculated for the WRF model output at 1000 UTC. Then these assumptions were gradually relaxed, one at time. At each step, the T_bs were re-computed, and the new T_bs were fed into the retrieval algorithm. By measuring the difference in T_bs between each step, along with the difference in values retrieved by the 1DVAR algorithm, one can isolate the effect of each assumption and gain insight into which sources of error are most significant. The results of this exercise are shown in Figures 4.3 and 4.4. Figure 4.3 shows the bias and root-mean-square errors induced at the five TEMPEST frequencies by each forward model error source, averaged across all pixels. Figure 4.4 shows the bias and RMS errors induced in the retrieved parameters of TPW, LWP, and IWP. Clear-sky and cloudy regimes are considered separately. Both plots show the effects at both nadir and a 45 degree view angle.

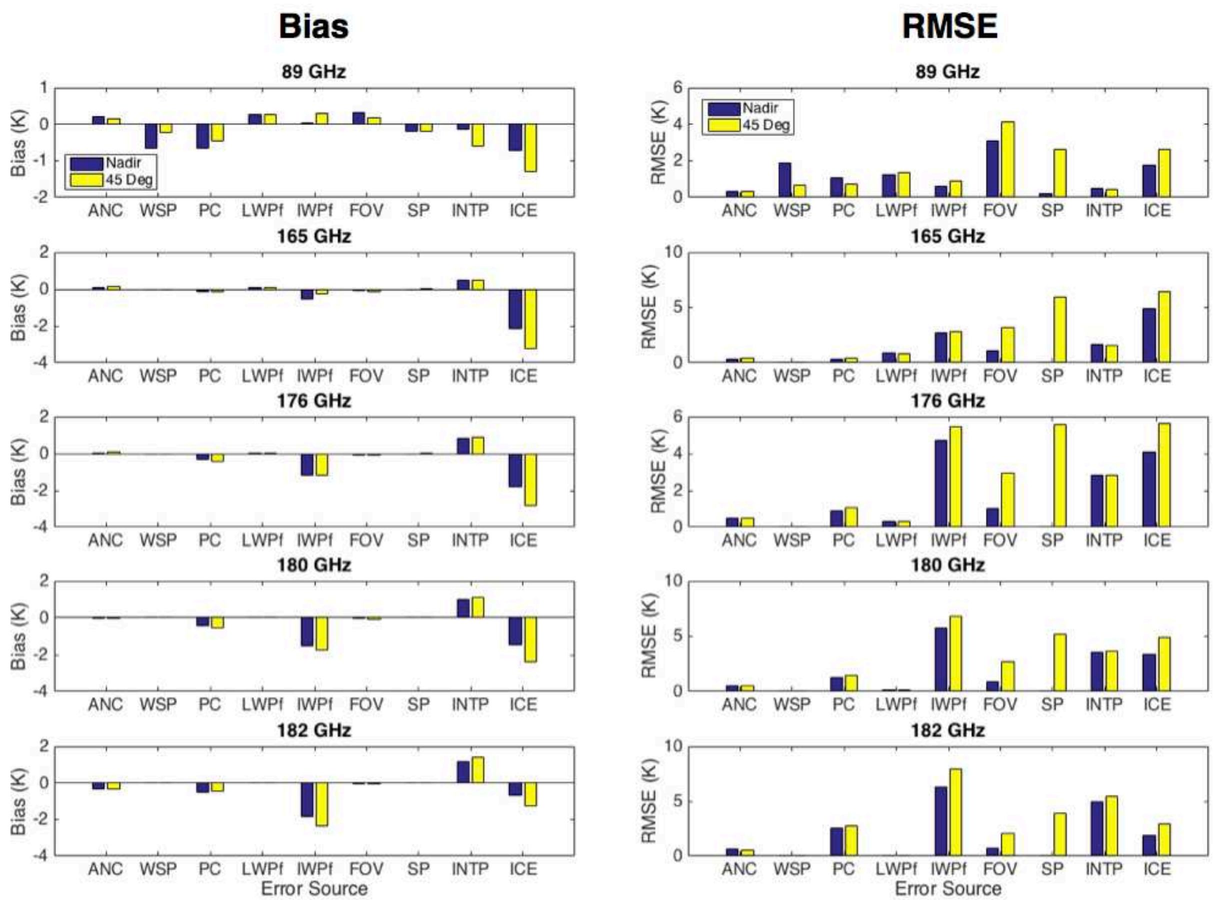

Figure 4.3. Bias (left) and RMS (right) errors in forward modeled TEMPEST brightness temperatures from various sources. Blue bars are errors at nadir and yellow bars errors at a 45° view angle. The errors sources considered are as follows: errors in ancillary atmospheric data (ANC), errors in assumed surface wind speed (WSP), limitations in the ability to represent the full water vapor profile with 3 principal components (PC), errors in the vertical distribution of liquid cloud drops (LWPf), errors in the vertical distribution of frozen hydrometeors (IWPf), errors induced by averaging over the full radiometer field of view (FOV), errors induced by the plane-parellel assumption (SP), errors induced by interpolating the 30-level WRF atmosphere to 16 levels (INTP), and errors in the assumed ice mircophysics (ICE).

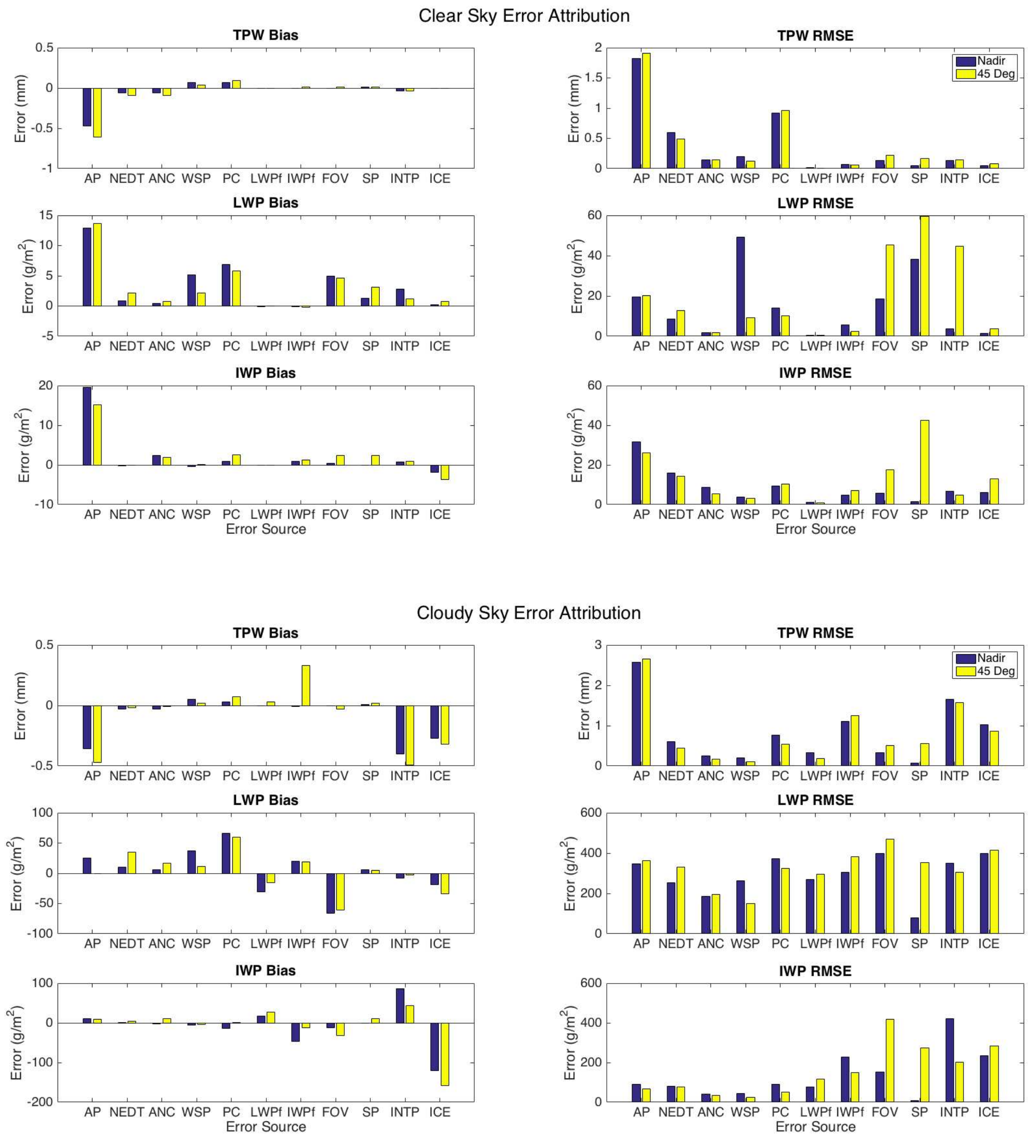

Figure 4.4. *Top left*: Biases in retrieved TPW, LWP, and IWP induced by error sources for clear-sky conditions. *Top right*: RMSE in clear-sky conditions. *Bottom right*: Cloudy-sky RMSE. *Bottom left*: Cloudy-sky biases. Blue bars are errors at nadir and yellow bars errors at a 45° view angle. The abbreviations are the same as for Fig. 4.3, with two extras: AP represents errors induced by a-priori assumptions, and NEDT represents errors induced by random errors in the radiometer observation.

A comparison of the magnitudes of the errors in Figure 4.4 shows which sources of error are most important for the various retrieved parameters, and the differences between the nadir and 45-degree error statistics offer insight into which assumptions contribute the most to the inconsistencies in the retrieval at high view angles.

4.2.1 Ancillary Data

Errors in the SST, surface pressure, height profile, and temperature profile assumed by the forward model are all small and thus are grouped together in this analysis. Mistaken assumptions about these variables lead to a small positive bias in 89 GHz T_b and a small negative bias at 182 GHz. Overall, though, induced errors are quite small and in most cases this source of forward model error can be safely ignored.

4.2.2 Surface Wind Speed

The surface wind speeds assumed by the forward model (taken from ERA5) are biased slightly low compared to the actual winds speed present in the WRF model. Since a lower wind speed translates to a lower surface emissivity, this bias in wind speed leads to a negative bias in 89 GHz T_b. The bias is larger at nadir than at 45 degrees, as one would expect given the greater sensitivity to the surface. When it comes to retrieved values, this bias in 89 GHz T_b is reflected in positively biased LWP values, because as discussed in Section 4.1, the LWP signal is also almost entirely at 89 GHz. Because the errors are larger at nadir, this effect is probably at least partly responsible for the fact that LWP values retrieved at 45 degrees tend to be lower. In the long run, of course, one would hope that assumed values of wind speed are unbiased. However, that doesn't change the fact that, for any given scene, assumed wind speeds are likely to have errors and that this error will affect the LWP retrieval.

4.2.3 Representation of the Water Vapor Profile

As mentioned in Chapter 2, it is impossible to capture the entire variability in possible water vapor profiles with only 3 principal components. Nevertheless, the forward model is restricted to adjusting the PC coefficients when trying to adjust the water vapor profile. This leads to considerable RMS errors in retrieved TPW in clear-sky regimes, probably mostly related to deficiencies in the way the lowest levels of the atmosphere, where most of the water vapor is located, are represented. For reasons that are not confidently understood at this time, the PC representation of the water vapor profile also contributes to a negative bias in 89 GHz brightness temperatures, and a corresponding positive bias in retrieved LWP. The response is similar across all view angles, however.

4.2.4 Placement of Cloud Liquid

This experiment confirms what was argued in Section 4.1; namely, that assuming a fixed liquid cloud level can lead to non-trivial errors in retrieved LWP, because of the different emission temperature. RMS errors due to this factor are on the order of 350 g/m^2, and are slightly higher at higher view angles. This assumption can be an important source of error in certain situations, but based on comparisons with the error statistics for the other assumptions, it is not necessarily a dominant source of error either.

4.2.5 Placement of Cloud Ice

The fixed distribution of frozen hydrometeors in the forward model creates negative biases at the 176, 180, and 182 GHz channels, as well as considerable RMS errors. This is probably because the forward model is putting ice in middle levels in the atmosphere more often than in the WRF model, which reduces the T_b depression at the channels that peak higher in the atmosphere. This leads to a negative bias in retrieved IWP. Although not nearly as important as ice microphysical assumptions, it is nonetheless a significant factor in the overall negative bias of retrieved IWP.

4.2.6 Field of View Size

The larger the field of view, the more likely it is that the FOV will include a mix of cloudy and clear areas. When comparing with a higher resolution product, the result of this sub-grid scale variability will be retrieved cloud fields that are biased high in clear areas and biased low in cloudy areas, as can be seen clearly in Figure 4.4. Even if all of the fields are averaged to a common low-resolution grid, differences remain. This is largely a consequence of the non-linear response of 89 GHz T_bs to increasing cloud water, and is closely related to the so-called beam-filling effect [e.g., *Greenwald et al.*, 1997]. Field of view errors are more of a problem for the retrieval of LWP than for IWP, which makes sense given the non-linearity of the LWP response and the face that the LWP retrieval relies heavily on the 89 GHz channel, which has lower resolution than the other channels. Given the large FOV-induced RMS errors, and the fact that these errors are significantly larger at 45 degrees (which makes sense, given the larger FOV), this is probably one of the most important factors contributing to view angle associated retrieval errors.

4.2.7 Plane-parallel Assumption

The plane-parallel assumption does not induce significant errors at nadir but can lead to substantial errors at 45 degrees. This does not result in significant biases, but retrievals at high view angles should be expected to be noisier in part due to this assumption.

4.2.8 Interpolation of Atmospheric Profiles

The forward model divides the atmosphere into 16 vertical levels, as opposed to the 30 levels specified by WRF, which leads to somewhat unexpectedly large errors. Probably the most significant errors are a positive bias in retrieved IWP and a negative bias in TPW in cloudy regions. The reasons for these biases are not entirely clear, but probably have to do with the decreased vertical resolution of the forward model above 300 hPa (where much of the ice is located) and insufficient resolution of the lower-level water vapor structure.

4.2.9 Ice Microphysical Assumptions

Unsurprisingly, the discrepancy between the habit and PSD of frozen hydrometeors in the forward model compared to the WRF model is by far the most important source of error in the retrieval of IWP. As has already been discussed, the forward model microphysics leads to an overestimation of the amount of scattering as compared to the WRF microphysics, which manifests itself in negative biases at all channels. Across all pixels, the 165 GHz T_bs are biased low by 2.15 K at nadir and by 3.25 K at 45 deg, with RMSE values of 4.92 K and 6.91 K, respectively. Although not shown in Fig. 4.4, if only pixels with IWP>500 g/m^2 are considered, these errors grow to over 15 K. This puts the forward model uncertainty in the brightness temperatures in line with the uncertainty estimates given in Section 2.4.1. The negative bias in the brightness temperatures leads to a large negative bias in retrieved IWP, consistent with Figure 3.1. It also results in smaller but still substantial negative biases in retrieved TPW and LWP in cloudy areas. In all cases, the effect is slightly stronger at higher view angles.

4.2.10 A-priori Selection and Sensor Noise

Figure 4.4 also includes two additional sources of retrieval errors, errors influenced by the choice of a-priori values as well as the random errors added to the synthetic T_bs to imitate radiometric noise. Sensor noise is relatively unimportant in the retrieval of TPW and IWP but does have a non-trivial effect on the LWP retrieval, acting to give a slightly positive LWP bias on the whole. The effect is larger at 45 degrees, reflecting the effect that there is less contrast in 89 GHz clear-sky and cloudy sky brightness temperatures at high view angles, meaning a given change in T_b will correspond to a larger change in retrieved LWP. The a-priori errors show the amount by which the retrieval is being dragged toward the a-priori state. This represents the largest source of error for the TPW retrieval. It is not a particularly important error term for the retrieval of LWP or IWP in cloudy conditions, but it does account for a lot of the positive bias in retrieved LWP and IWP in clear-sky regions.

4.3 Error Mitigation with Coincident Satellite Observations

Some of the errors examined in the previous section could be constrained if a TEMPEST series of observations were to take place near the time of an observation by a different spaceborne instrument. For example, most of the passive microwave radiometers in the GPM constellation include a channel near 37 GHz. This channel is more sensitive to liquid cloud water than 89 GHz and does not saturate as quickly, making retrievals of LWP more accurate. While it would be hard to add a 37 GHz channel to the TEMPEST instrument, due to the large antenna size required and the size limitations of the CubeSat platform, anytime a TEMPEST observation is made in close proximity to a retrieval of LWP from one of these other satellites, that a-priori information could be used to further constrain the TEMPEST retrieval of LWP. This would particularly improve retrieval performance in areas of high LWP, where the 89 GHz channel on TEMPEST saturates, and would help reduce the differences in retrieved LWP between high and low view angles. The 37 GHz channel, along with even lower frequency channels on GMI and AMSR-2, can also be used to retrieve wind speeds. The incorporation of these more accurate wind speeds into the retrieval, instead of relying on reanalysis data, would also serve to improve the LWP retrieval.

Observations made near the same time as the “A-Train” series of satellites offer even more possibilities for improving the retrieval. In addition to the AMSR-2 microwave radiometer, the A-Train includes two instruments, the Advanced Microwave Sounding Unit (ASMU-A) and the Atmospheric Infrared Sounder (AIRS), which could help further constrain the water vapor profile. More accurate water vapor a-priori assumptions, particularly near the surface, would reduce the errors associated with the principal component representation of water vapor in the forward model. Also, the A-train contains the CloudSat cloud radar, as well as the Cloud-Aerosol Lidar with Orthogonal Polarization (CALIOP) on the CALIPSO satellite. Observations from these instruments, while limited to a narrow swath with a width of less than 2 km for CloudSat and less than 100 m for CALIOP, could be used to provide the TEMPEST retrieval with a more accurate picture of the heights and depths of the clouds being observed. As laid out in Section 4.2, the forward model’s simplified vertical distribution of cloud liquid and cloud ice represent two of the most sizable sources of forward model error, so being able to adjust these cloud heights to match nearby radar and lidar observations would be of great benefit. The information from CloudSat and CALIPSO could also help to better constrain the frozen hydrometeor PSD. Thus, the detailed information provided by the A-train instruments could help constrain the forward model for a given cloud system, allowing for more accurate TEMPEST retrievals by the oreceeding or subsequent instruments in the TEMPEST cluster, which in turn would add value to the A-train observations by providing temporal context.

Geostationary satellite observations could also potentially be used to reduce errors in the retrieval, without having to rely on coincident overpasses that occur only a few times per day. For example, the Advanced Baseline Imager (ABI) on GOES-16 can be used to identify cloudy areas and estimate cloud-top heights and cloud-top particle size. This would allow for stricter a-priori errors in LWP and IWP to be assumed, reducing the positive bias in these values in clear-sky regimes; and incorporating the information about cloud height and particle size into the forward model could help reduce errors associated with the assumed cloud levels and ice microphysics. ABI information could potentially be leveraged quite productively with a TEMPEST mission, since it also has a temporal resolution of 5 minutes, while the TEMPEST radiometers would add information critical to the understanding of cloud process by virtue of their ability to see through the cloud tops to better understand changes inside the cloud itself.

Finally, it is worth noting that once a sufficient number of coincident measurements have been made, covering the full diurnal cycle and a wide geographic area, these observations could be used to train the retrieval algorithm and improve performance even when coincident observations are not available. For example, statistics relating the cloud morphology and cloud top temperatures observed by ABI to the parameters retrieved by TEMPEST could be used to develop a forward model that makes assumptions that are not fixed for all pixels but rather depend somewhat on the atmospheric state.

CHAPTER 5: CONCLUSIONS AND FUTURE WORK

A robust, physically based optimal estimation retrieval algorithm has been developed for use with TEMPEST-D and other similar cross-track sounders. The algorithm can be used to retrieve a rough vertical profile of water vapor as well as integrated amounts of liquid cloud water and cloud ice/snow at view angles ranging from nadir to 45 degrees. The primary goal of this study was to determine the extent to which view angle differences might hamper the utility of a proposed cluster of closely spaced TEMPEST CubeSats. Synthetic observations generated from a high-resolution WRF simulation indicate that, in most cases, the errors in retrieved parameters introduced by view angle differences are small enough that the true atmospheric signal can be distinguished from the noise. This is especially true for observations made between nadir and about 30 degrees, where field of view changes are more gradual. Nevertheless, view angle related errors should not be ignored, and it is worth considering ways in which both the retrieval algorithm as well as the TEMPEST mission concept itself could be refined.

While the forward model is able to partly adjust for the changing nature of retrievals at different view angles, through its use of a view-angle-dependent forward model error covariance matrix, deficiencies remain. The retrieval of LWP at high view angles becomes particularly problematic, due to the reduced sensitivity at the 89 GHz channel. However, in the context of a fleet of closely spaced radiometers, using higher quality near-nadir retrievals for a-priori information can eliminate a significant fraction of this error, while still allowing the retrieval to discern true changes in atmospheric state. This iterative approach to refining the a-priori state vector and assumed errors also improves performance in the retrieval of IWP, though to a lesser extent. It is worth a more careful examination of how additional sources of a-priori information, perhaps from coincident overpasses of other low Earth orbit satellites or even infrared radiances from geostationary satellite instruments, could further constrain the retrieval. Better constrains on the surface wind speed, as well as the placement of cloud levels, would undoubtedly reduce errors in the retrieved parameters.

Another important source of discrepancies between low and high view angle retrievals is the change in field of view. Studies have been conducted [e.g., *Bremen et al.*, 2002; *Hilburn and Wentz*, 2008] to try to quantity and correct for beamfilling errors, and it would probably be helpful to try to implement a similar correction in the TEMPEST retrieval algorithm. Information from geostationary satellites could also be used to identify the fraction of area within a given field of view that is cloudy.

In addition, changes to the mission concept could be considered that might help reduce errors induced by changing view angles. For example, this study shows that the errors in the retrieval start to increase more rapidly past view angles of about 30 degrees. This suggests it might be beneficial to space the TEMPEST CubeSats more closely together than the 6-minute spacing assuming in this experiment. With closer spacing, more observations of the same location would be able to be performed at view angles near nadir. In addition, field of view differences between successive overpasses would be smaller, and the closer spacing would allow for stricter assumed a-priori errors that might improve performance even at high view angles. The tradeoff, of course, is that more CubeSats would be required in order to cover the same length of time.

A related consideration is that, at higher latitudes, the rotation speed of a given point on the Earth is reduced, so for a given TEMPEST spacing, the change in view angle between observations will be lessened. Additionally, locations outside the tropics tend not to have TPW values that are as high as some of the extreme values seen in this hurricane simulation, which could increase the sensitivity to cloud water. Given these facts, it is possible that more consistent retrievals could be obtained away from the tropics.

Finally, it is worth considering whether a TEMPEST mission would be better served by a different combination of channels. The channels chosen for the TEMPEST-D instrument allow for reliable retrievals of atmospheric water vapor in clear skies (see Appendix), and are beneficial in that the similarities with channels on other spaceborne passive microwave radiometers allow for easier calibration once in orbit. However, clear-sky water vapor does not tend to change very rapidly with time, and so the benefits of having a train of closely spaced observations accrue mostly in cloudy cases, where the water vapor retrieval does not have much skill. In addition, the only TEMPEST-D channel with a sensitivity to cloud liquid is the 89 GHz channel, and going to lower frequencies where the sensitivity is stronger is problematic due to antenna size and FOV issues. This suggests that the TEMPEST mission might be most successful if it were to focus on ice processes in clouds. However, more useful information about cloud ice could be obtained if the observing frequencies were spaced farther apart. Because four of the TEMPEST channels operate at similar frequencies, the scattering signature of a frozen particle of a given size and habit will be similar across all channels – that is, the channels do not actually represent four independent sources of information. In addition, small ice particles do not create much of a scattering signature at these frequencies. The hypothetical inclusion of higher frequency channels on a TEMPEST CubeSat, even if it were at the expense of existing channels, would lead to increased sensitivity to small ice particles and a greater ability to distinguish between particle habits and size distributions. While a more careful study is warranted before any re-design of the radiometer, work by *Birman et al.* [2017] examining the information content of a wide range of microwave frequencies suggests that the retrieval of cloud ice and snow would benefit most from the inclusion of channels near 874 GHz, 664.2 GHz, and 251 GHz. Similar improvements could possibly achieved by interspersing separate radiometers such as Tropospheric Water and cloud ICE (TWICE) CubeSat instruments [*Jiang et al*., 2017] within the TEMPEST constellation.

Ultimately, one of the main goals of the TEMPEST mission is to improve cloud parameterizations in models. This work has demonstrated that changes in integrated amounts of cloud liquid and cloud ice could be retrieved from a TEMPEST fleet, but has not explicitly shown how one might use this information to constrain parameters such as the graupel collection efficiency or autoconversion threshold radius mentioned in Chapter 1. In fact, given that the sensitivity to liquid is limited to only one TEMPEST channel, it might be the case that more progress can be made with respect to ice-phase parameterizations. For example, *Elsaesser et al.* [2017] found that a more realistic partitioning of convective ice into precipitating and detrained condensate could be obtained in a GCM by incorporating a new convective ice parameterization scheme informed by aircraft field campaigns. The question of how much ice is detrained from convective updrafts is important because convective anvils have important radiative effects and can affect climate sensitivity [*Lindzen et al.*, 2001]. Direct observations by a TEMPEST fleet of the ice mass flux from convective cores into surrounding anvil clouds could further constrain convective ice parameterizations, especially in regimes not including in the aircraft field campaigns.

More work is needed to determine the best way to make use of TEMPEST observations, and collaboration with the modeling community will be critical in paving the way forward. While the idea of improving cloud model parameterizations by way of cloud process observations from TEMPEST remains a long-term goal, this study has advanced our understanding of the nature of the challenges involved and points toward multiple avenues by which some of these challenges might be mitigated. The fact that changes in LWP and IWP can be reliably retrieved, even at different view angles and for closely-spaced observations, indicates that this novel observation concept holds great promise.

REFERENCES

Adams-Selin, R. D., S. C. van den Heever, and R. H. Johnson, 2013: Impact of graupel parameterization schemes on idealized bow echo simulations. *Mon. Weather Rev.*, **141**, 1241-1262.

Alishouse, J. C., S. A. Snyder, J. Vongsathorn, and R. R. Ferraro, 1990: Determination of oceanic total precipitable water from the SSM/I. *IEEE Trans. Geosci. Remote Sens.*, **28**, 811-816.

Bennartz, R., 2007: Global assessment of marine boundary layer cloud droplet number concentration from satellite. *J. Geophys. Res.*, **112**, D02201.

Birman, C., J.-F. Mahfouf, M. Milz, J. Mendrok, S. A. Buehler, and M. Brath, 2017: Information content on hydrometeors from millimeter and sub-millimeter wavelengths. *Tellus A*, **69:1**, 1271562.

Boukabara, S. A., et al., 2011: MiRS: An all-weather 1DVAR satellite data assimilation and retrieval system. *IEEE Trans. Geosci. Remote Sens.*, **49**, 3249-3272.

Bremen, L. V., E. Ruprecht, and A. Macke, 2002: Errors in liquid water path retrieval arising from cloud inhomogeneities: The beam-filling effect. *Meteor. Z.*, **11**, 13–19.

Cintineo, R., J. A. Otkin, M. Xue, and F. Kong, 2014: Evaluating the performance of planetary boundary layer and cloud microphysical parameterization schemes in convection-permitting ensemble forecasts using synthetic GOES-13 satellite observations. *Mon. Weather Rev.*, **142**, 163-182.

Deblonde, G., and S. English, 2003: One-dimensional variation retrievals from SSMIS-simulated observations. *J. Appl. Meteorol.*, **42**, 1406-1420.

Draine, B. T., and P. J. Flatau, 1994: Discrete-dipole approximation for scattering calculations. *J. Opt. Soc. Amer.*, **11**, 1491-1499.

Duncan, D. I., and C. D. Kummerow, 2016: A 1DVAR retrieval applied to GMI: Algorithm description, validation, and sensitivities. *J. Geophys. Res. Atmos.*, **121**, 7415-7429.

Elsaesser, G. S., and C. D. Kummerow, 2008: Toward a fully parametric retrieval of the nonraining parameters over the global oceans. *J. Appl. Climatol.*, **47**, 1599-1618.

___, A. D. Del Genio, J. H. Jiang, and M. van Lier-Walqui, 2017: An Improved Convective Ice Parameterization for the NASA GISS Global Climate Model and Impacts on Cloud Ice Simulation. *J. Climate*, **30**, 317-336.

Field, P. R., R. J. Hogan, P. R. A. Brown, A. J. Illingworth, T. W. Choularton, and R. J. Cotton, 2005: Parameterization of ice-particle size distributions for mid-latitude stratiform cloud. *Quart. J. Roy. Meteor. Soc.*, **131**, 1997-2017.

___, A. J. Heymsfield, and A. Bansemer, 2007: Snow size distribution parameterization for midlatitude and tropical ice clouds. *J. Atmos. Sci*., **64**, 4346-4364.

Golaz, J.-C., J. Salzmann, L. J. Donner, L. W. Horowitz, Y. Ming, and M. Zhao, 2011: Sensitivity of the aerosol indirect effect to sub-grid variability in the cloud parameterization of the GFDL Atmosphere General Circulation Model AM3. *J. Climate*, **24**, 3145-3160.

___, L. W. Horowitz, and H. Levy II, 2013: Cloud tuning in a coupled climate model: Impact on 20th century warming. *Geophys. Res. Let*., **40**, 2246-2251.

Greenwald, T. J., G. L. Stephens, T. H. Vonder Haar, and D. L. Jackson, 1993: A physical retrieval of cloud liquid water over the global oceans using special sensor microwave / imager (SSM/I) observations. *J. Geophys. Res. Atmos*., **98**, 18,471-18,478.

___, S. A. Christopher, and J. Chou, 1997: Cloud liquid water path comparisons from passive microwave and solar reflectance measurements: Assessment of subfield-of-view cloud effects in microwave retrievals. *J. Geophys. Res.*, **102**, 19585-19596.

Heymsfield, A. J., and L. J. Donner, 2000: A scheme for parameterizing ice cloud water content in general circulation models. *J. Atmos. Sci.*, **47**, 1865-1877.

___, and J. Iaquinta, 2000: Cirrus crystal terminal velocities. *J. Atmos. Sci*., **57**, 916-938.

Hilburn, K. A., and F. J. Wentz, 2008: Intercalibrated Passive Microwave Rain Products from the Unified Microwave Ocean Retrieval Algorithm (UMORA). *J. Appl. Meteor. Climatol.*, **47**, 778-794.

Hong, G., 2007: Parameterization of scattering and absorption properties of nonspherical ice particles at microwave frequencies. *J. Geophy. Res.*, **112**, D11208.

Jiang, J. H., et al., 2017: A simulation of ice cloud particle size, humidity and temperature measurements from the TWICE CubeSat. Earth and Space Science, **4**, 574-587.

Johnson, J. S., Z. Cui, L. A. Lee, J. P. Gosling, A. M. Blyth, and K. S. Carslaw, 2015: Evaluating uncertainty in convective cloud microphysics using statistical emulation. J. *Adv. Model. Earth Syst.*, **7**, 162-187.

Kawamoto, K., T. Nakajima, and T. Y. Nakajima, 2001: A global determination of cloud microphysics with AVHRR remote sensing. *J. Climate*, **14**, 2054-2068.

Kazumori, M., and S. J. English, 2015: Use of the ocean surface wind direction signal in microwave radiance assimilation. *Q. J. R. Meterol. Soc.*, **141**, 1354-1375.

Kim, M.-J., M. S. Kulie, C. O'Dell, and R. Bennartz, 2007: Scattering of ice particles at microwave frequencies: A physically based parameterization. *J. Appl. Meteor. Climatol*., **46**, 615-633.

Khain, A. P., M. Ovtchinnikov, M. Pinsky, A. Prokrovsky, and H. Krugliak, 2000: Notes on the state-of-the-art numerical modeling of cloud microphysics. *Atmos. Res.*, **55**, 159-224.

Kulie, M. S., R. Bennartz, T. Greenwald, Y. Chen, and F. Weng, 2010: Uncertainties in microwave properties of frozen precipitation: Implications for remote sensing and data assimilation. *J. Atmos. Sci*., **67**, 3471-3487.

Lambrigsten, B., W. Wilson, A. Tanner, T. Gaier, C. Ruf, and J. Piepmeier, 2004: GeoSTAR – A microwave sounder for geostationary satellites. *Proc. IGARSS*, **2**, 777-780.

Lee, G., I. Zawadzki, W. Szyrmer, D. Sempere-Torres, and R. Uijlenhoet, 2004: A general approach to double-moment normalization of drop size distributions. *J. Appl. Meteor.*, **43**, 264-281.

Liebe, H. J., G. A. Hufford, and T. Manabe, 1991: A model for the complex permittivity of water at frequencies below 1 THz. *Int. J. Infrared Millimeter Waves*, **12**, 659-675.

Lindzen, R.S., M.-D. Chou, and A. Y. Hou, 2001: Does the Earth have an adaptive infrared iris? *Bull. Amer. Meteor. Soc.*, **82** (3), 417-432.

Lim, K.-S. S., and S.-Y. Hong, 2010: Development of an effective double-moment cloud microphysics scheme with prognostic cloud condensation nuclei (CCN) for weather and climate models. *Mon. Weather Rev.*, **138**, 1587-1612.

Liu, G., 2008: A database of microwave single-scattering properties for nonspherical ice particles. *Bull. Amer. Meteor. Soc.*, **89**, 1563-1570.

Lohmann, U., and J. Feichter, Impact of sulfate aerosols on albedo and lifetime of clouds: A sensitivity study with the ECHAM4 GCM. *J. Geophys. Res.*, **102**, 13,685-13,700.

Nowell, H., G. Liu, and R. Honeyager, 2013: Modeling the single-scattering properties of aggregate snowflakes, *J. Geophy. Res. Atmos.*, **118**, 7873-7885.

Matzler, C., P. W. Rosenkranz, and J. Cermak, 2010: Microwave absorption of supercooled clouds and implications for the dielectric properties of water. *J. Geophys. Res.,* **155**, D23208.

Michalakes, J., S. Chen, J. Dudhia, L. Hart, J. Klemp, J. Middlecoff, and W. Skamarock, 2001: Development of a next generation regional weather research and forecast model. *Developments in Teracomputing: Proceedings of the Ninth ECMWF Workshop on the Use of High Performance Computing in Meteorology.* Eds. Walter Zwieflhofer and Norbert Kreitz, World Scientific, 269-276.

Morrison, H., A. Morales, and C. Villanueva-Birriel, 2015: Concurrent sensitivities of an idealized deep convective storm to parameterizations of microphysics, horizontal grid resolution, and environmental static stability. *Mon. Weather Rev*., **143**, 2082-2104.

Pawlowska, H., and J.-L. Brenguier, 2003: An observational study of drizzle formation in stratocumulus clouds for general circulation model (GCM) parameterizations. *J. Geophys. Res*., **108**(D15), 8630, 13.

Petty, G. W., and W. Huang, 2010: Microwave backscatter and extinction by soft ice spheres and complex snow aggregates. *J. Atmos. Sci.*, **67**, 769-787.

Reising, S. C., et al., 2017: Temporal Experiment for Storms and Tropical Systems Technology Demonstration (TEMPEST-D) Mission: Enabling time-resolved cloud and precipitation observations from 6U-class satellite constellations. Proc. 31st AIAA/USU Conference on Small Satellites, Logan, UT, August 5-10, 2017, SSC17-III-01.

Reisner, J., R. M. Rasmussen, and R. T. Bruintjes, 1998: Explicit forecasting of supercooled liquid water in winter storms using the MM5 mesoscale model. *Quart. J. Roy. Meteor. Soc*., **124**, 1071-1107.

Rodgers, C. D., 2000: *Inverse Methods for Atmospheric Sounding: Theory and Practice*. World Scientific Publishing Co., Singapore, 238 pp.

Rosenkranz, P. W., 1998: Water vapor microwave continuum absorption: A comparison of measurements and models. *Radio Sci.*, **33**, 919-928.

Rotstayn, L. D., 2000: On the cloud "tuning" of autoconversion parameterizations in climate models. *J. Geophys. Res*., **105**(D12), 15,495-15,507.

Rutledge, S. A., and P. V. Hobbs, 1983: The mesoscale and microscale structure and organization of clouds and precipitation in midlatitude cyclones, VIII: A model for the "seeder-feeder" process in warm-frontal rainbands. *J. Atmos. Sci*., **40**, 1185-1206.

Saleeby, S. M. and W. R. Cotton, 2008: A binned approach to cloud droplet riming implemented in a bulk microphysics model. *J. Appl. Meteor. Climatol.*, **47**, 694-703.

Staelin, D. H., A. H. Barrett, J. W. Waters, F. T. Barath, E. J. Johnston, P. W. Rosenkranz, N. E. Graut, and W. B. Lenoir, 1973: Microwave Spectrometer on the Nimbus 5 Satellite: Meteorological and Geophysical Data. *Science*, **182**, 1339-1341.

Suzuki, K., T. Y. Nakajima, and G. L. Stephens, 2010: Particle growth and drop collection efficiency of warm clouds as inferred from join *CloudSat* and MODIS observations. *J. Atmos. Sci.*, **67**, 3019-3032.

___, G. L. Stephens, S. C. Van Den Heever, and T. Y. Nakajima, 2011: Diagnosis of the warm rain process in cloud-resolving models using joint *CloudSat* and MODIS observations. *J. Atmos. Sci.*, **68**, 2655-2670.

___, J.-C. Golaz, and G. L. Stephens, 2013: Evaluating cloud tuning in a climate model with satellite observations. *Geophys. Res. Let*., **40**, 4464-4468.

Van Weverberg, K., A. M. Vogelmann, W. Lin, E. P. Luke, A. Cialella, P. Minnis, M. Khaiyer, E. R. Boer, and M. P. Jensen, 2013: The role of cloud microphysics parameterization in the simulation of mesoscale convective system clouds and precipitation in the Tropical Western Pacific. *J. Atmos. Sci*., **70**, 1104-1127.

von Blohn, N., K. Kiehl, S. K. Mitra, and S. Borrmann, 2009: Riming of graupel: Wind tunnel investigations of collection kernels and growth regimes. *J. Atmos. Sci*., **66**, 2359-2366.

Wentz, F. J, 1997: A well-calibrated ocean algorithm for special sensor microwave / imager. *J. Geophys. Res.*, **102**, 8703-8718.

Wilheit, T. T., and A. T. C. Chang, 1980: An algorithm for retrieval of ocean's surface and atmospheric parameters from the observations of the Scanning Multichannel Microwave Radiometer. *Radio Sci.,* **15**, 525-544.

Zhao, L. M., and F. Z. Weng, 2002: Retrieval of ice cloud parameters using the Advanced Microwave Sounding Unit. *J. Appl. Meteor*., **41**, 384-395.

APPENDIX: CLEAR SKY WATER VAPOR PROFILE RETRIEVAL

While not critical to the TEMPEST mission concept, the same optimal estimation framework developed in this thesis can be used to retrieve information about the water vapor content of the atmosphere from TEMPEST-D or any cross-track radiometer operating at similar frequencies, such as MHS or ATMS. Moreover, for calibration purposes, it is important that TEMPEST radiometers be able to properly interpret water vapor in the atmosphere. Then, if the radiometer were to start to malfunction while in-orbit, this would manifest itself in higher χ^2 values that could be rapidly detected. Here, we test the performance of the water vapor retrieval algorithm in clear-sky conditions, and the consistency across different view angles.

The clear-sky retrieval algorithm is the same as the all-sky algorithm, with the important exception that the assumed errors that make up the forward model error covariance matrix $\boldsymbol{S_y}$ are much smaller. This is appropriate because changes in the water vapor profile have a smaller effect on T_bs than do changes in clouds. A more restrictive $\boldsymbol{S_y}$ allows the retrieval to converge on the true water vapor profile more closely while being less closely tied to a-priori assumptions. This clear sky $\boldsymbol{S_y}$ is created in the same manner describe in Section 2.4.3, except only WRF simulation pixels that are clear of any clouds are included in the calculation. As for the all-sky retrieval algorithm, different error covariance matrices are calculated for all possible view angles, in five-degree increments.

To test the clear-sky retrieval algorithm, hourly data from the WRF Hurricane Gonzalo simulation, *with all cloud water, rain, ice, snow, and hail artificially removed*, were used to create synthetic brightness temperatures, in the same manner described in Section 2.3. These synthetic T_bs were then used to retrieve the coefficients for the principal components of the water vapor profile, while the LWP and IWP parameters in the forward model were held fixed at zero. The a-priori water vapor profile was taken from ERA5, as in the all-sky retrieval.

Figure A.1 shows sample retrievals of TPW at nadir and 45 degrees for WRF output at 1200 UTC. Also shown is the TPW from the model as well as from ERA5. Of course, the large FOV of the TEMPEST radiometer, compared to the resolution of the model output, makes it impossible to capture features at the finest scales, but overall the retrieval does a good job of reproducing the TPW, with the main exception being the area near the core of the hurricane. The water vapor profile in this area probably shouldn't be considered to be very similar to those found in true clear-sky conditions, however. The retrieval shows clear improvement over the a-priori TPW values, a fact illustrated in Figure A.2. Outside of the hurricane core, errors in TPW are much smaller for the retrieval than for ERA5, indicating that there is a radiometric signal in clear skies with which to retrieve information about vertically integrated water vapor amounts. The pattern of errors in Figure A.2 does show residual a-priori influence, with positive biases tending to occur in areas where the a-priori TPW is positively biased, and negative biases where the a-priori errors are also negative. The patchy appearance of the error fields points to the influence of the (artificially-imposed) sensor noise as well.

Notably, the pattern of errors at nadir and at 45° are quite similar, demonstrating the stability of the retrieval across the full range of view angles considered. Figure A.3 plots the TPW bias, correlation coefficient, and RMSE as a function of view angle, for the full simulation. The bias in the retrieved TPW ranges from a minimum of 0.18 (at 45°) to a maximum of 0.27 mm (at 30°). These biases are much smaller in magnitude than the a-priori bias of -1.40. The correlation coefficient is between 0.956 and 0.964 at all view angles, an improvement over the ERA5 correlation of 0.916, and the RMS errors are between 2.05 and 2.14 mm, compared to

3.08 for ERA5. Based on these statistics, it does not appear that view angle differences should be a major source of concern for the clear-sky water vapor retrieval.

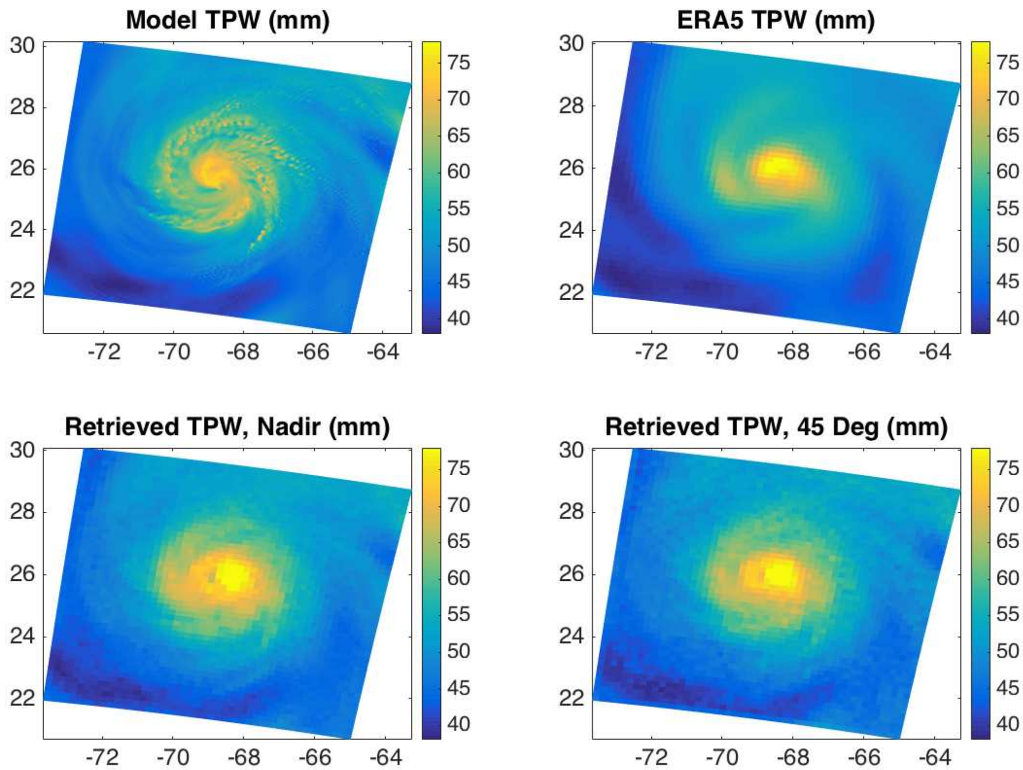

Figure A.1. *Top left:* Total precipitable water from the WRF Hurricane Gonzalo simulation at 1200 UTC, at 3km resolution. *Top right*: TPW from ERA5 reanalysis at 1200 UTC. *Bottom right*: TPW retrieved by the optimal estimation algorithm, assuming a view angle of 45 degrees. *Bottom left*: TPW retrieved at nadir.

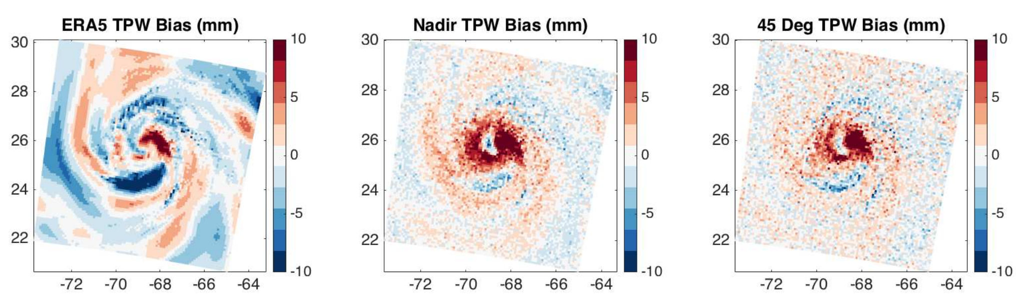

Figure A.2. Difference between retrieved TPW and model TPW for retrievals made at nadir (middle) and a 45° view angle (right). The difference between ERA5 and model TPW is also shown for reference (left).

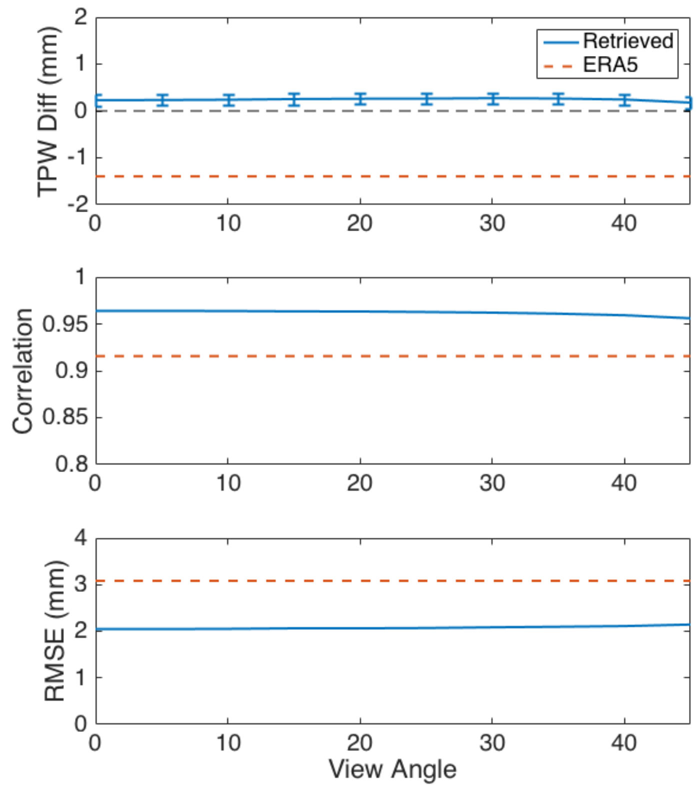

Figure A.3. *Top*: Average retrieved minus model TPW, as a function of view angle (blue solid line), along with the constant ERA5 bias (red dashed line). Error bars represent $\pm$ 1 standard error, assuming an effective sample size of n/100 to account for spatial autocorrelation. *Middle*: Correlation coefficient between the retrieved and model TPW as a function of view angle, along with the ERA5 correlation coefficient. *Bottom*: Root-mean-squared error of the retrieved TPW values as a function of view angle, along with the ERA5 RMSE.

Lastly, since the optimal estimation algorithm retrieves principal components of variation about a mean profile, it is possible to obtain rough information about the vertical structure of the water vapor profile. Figure A.4 shows the water vapor mixing ratios in the WRF simulation at 1200 UTC for the levels of 500 hPa and 900 hPa. Also shown are the mixing ratios implied by the retrieved PC coefficients, and the corresponding mixing ratio from ERA5. It is clear that the retrieval is able to discern the structure of the water vapor profile more accurately in the middle part of the troposphere than near the surface. This is likely due to two factors. First, as shown in

Figure 4.1, the channel weighting functions are more sensitive to the middle atmosphere, particularly in moist environments. Second, the principal components used by the algorithm, while optimized to explain the maximum amount of the total variance in the water vapor profile, are not necessarily optimized to explain the maximum amount of variance in the near-surface water vapor. Figure 2.4 shows that all of the principal components are rather close to zero near the surface. This means that stark variations in mixing ratio in the lower levels cannot be properly represented using the three PCs. Depending on the desired application, it might be useful to use different PCs to capture more of the low-level variance, but this would likely come at the expense of accuracy at other levels.

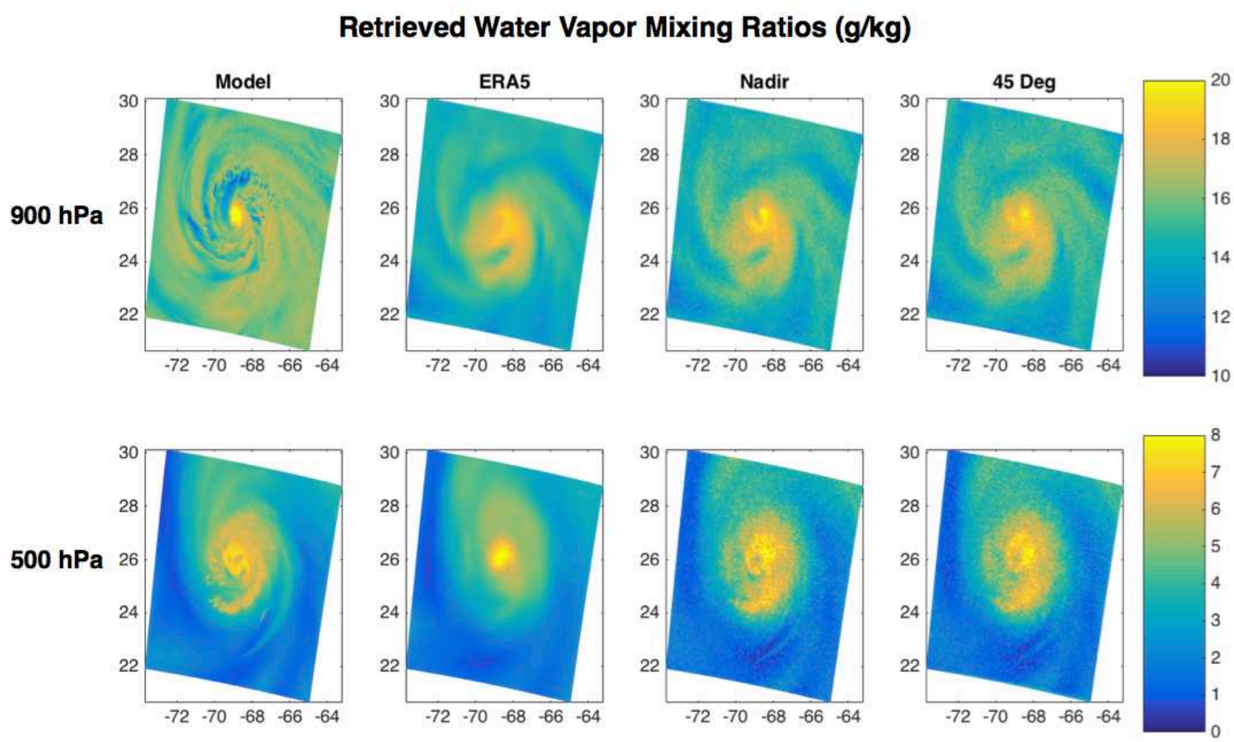

Figure A.4. Water vapor mixing ratio at 900 hPa (top row) and 500 hPa (bottom row) for the WRF model at 1200 UTC and corresponding fields for ERA5 and synthetic TEMPEST retrievals at nadir and 45 degrees.